OPEN ACCESS Freely available online

PLoS COMPUTATIONAL BIOLOGY

Efficacy of Synaptic Inhibition Depends on Multiple, Dynamically Interacting Mechanisms Implicated in Chloride Homeostasis

Nicolas Doyon[1,2], Steven A. Prescott[3], Annie Castonguay[1,2], Antoine G. Godin[1], Helmut Kröger[4], Yves De Koninck[1,2]*

1 Division of Cellular and Molecular Neuroscience, Centre de recherche Université Laval Robert-Giffard, Québec, Québec, Canada, **2** Department of Psychiatry & Neuroscience, Université Laval, Québec, Québec, Canada, **3** Department of Neurobiology and Pittsburgh Center for Pain Research, University of Pittsburgh, Pittsburgh, Pennsylvania, United States of America, **4** Department of Physics, Université Laval, Québec, Québec, Canada

Abstract

Chloride homeostasis is a critical determinant of the strength and robustness of inhibition mediated by $GABA_A$ receptors ($GABA_A$Rs). The impact of changes in steady state Cl^- gradient is relatively straightforward to understand, but how dynamic interplay between Cl^- influx, diffusion, extrusion and interaction with other ion species affects synaptic signaling remains uncertain. Here we used electrodiffusion modeling to investigate the nonlinear interactions between these processes. Results demonstrate that diffusion is crucial for redistributing intracellular Cl^- load on a fast time scale, whereas Cl^-extrusion controls steady state levels. Interaction between diffusion and extrusion can result in a somato-dendritic Cl^- gradient even when KCC2 is distributed uniformly across the cell. Reducing KCC2 activity led to decreased efficacy of $GABA_A$R-mediated inhibition, but increasing $GABA_A$R input failed to fully compensate for this form of disinhibition because of activity-dependent accumulation of Cl^-. Furthermore, if spiking persisted despite the presence of $GABA_A$R input, Cl^- accumulation became accelerated because of the large Cl^- driving force that occurs during spikes. The resulting positive feedback loop caused catastrophic failure of inhibition. Simulations also revealed other feedback loops, such as competition between Cl^- and pH regulation. Several model predictions were tested and confirmed by $[Cl^-]_i$ imaging experiments. Our study has thus uncovered how Cl^- regulation depends on a multiplicity of dynamically interacting mechanisms. Furthermore, the model revealed that enhancing KCC2 activity beyond normal levels did not negatively impact firing frequency or cause overt extracellular K^- accumulation, demonstrating that enhancing KCC2 activity is a valid strategy for therapeutic intervention.

Citation: Doyon N, Prescott SA, Castonguay A, Godin AG, Kröger H, et al. (2011) Efficacy of Synaptic Inhibition Depends on Multiple, Dynamically Interacting Mechanisms Implicated in Chloride Homeostasis. PLoS Comput Biol 7(9): e1002149. doi:10.1371/journal.pcbi.1002149

Editor: Abigail Morrison, University of Freiburg, Germany

Received December 24, 2010; **Accepted** June 11, 2011; **Published** September 8, 2011

Funding: This research was supported by the Natural Sciences and Engineering Research Council (NSERC) of Canada (YDeK) and by the National Institutes of Health, RO1 NS063010 (SAP). ND was supported by postdoctoral fellowships from NSERC and the Neurophysics training program funded by the Canadian Institutes of Health Research. SAP is a Rita Allen Foundation Scholar in Pain and the 53rd Mallinckrodt Scholar. AC was supported by a postdoctoral fellowship from Fonds de la Recherche en Santé du Québec (FRSQ). Y De K is a Chercheur National of the FRSQ. The funders had no role in study design, data collection and analysis, decision to publish, or preparation of the manuscript.

Competing Interests: The authors have declared that no competing interests exist.

* E-mail: yves.dekoninck@crulrg.ulaval.ca

Introduction

In the central nervous system, fast inhibition is mediated by $GABA_A$ and glycine receptor-gated Cl^- channels ($GABA_A$R and GlyR). Influx of Cl^- through these channels produces outward currents that cause hyperpolarization or prevent depolarization caused by concurrent excitatory input (*i.e.* shunting) [1,2]. Hyperpolarization and shunting both typically reduce neuronal spiking. However, Cl^- influx through $GABA_A$R necessarily increases $[Cl^-]_i$, which in turn causes depolarizing shifts in the Cl^- reversal potential (E_{Cl}) [3,4]. As the Cl^- gradient is depleted and E_{Cl} rises, the efficacy of $GABA_A$R-mediated control of spiking is compromised [5]. Therefore, mechanisms that restore the transmembrane Cl^- gradient are crucial for maintaining the efficacy of $GABA_A$R-mediated inhibition.

Cation-chloride cotransporters (CCCs) play a key role in maintaining the Cl^- gradient across the membrane [6,7]. Most relevant to neurons are the Na^+-K^+-$2Cl^-$ cotransporter (NKCC1), which normally mediates uptake of Cl^- [8], and the K^+-Cl^- cotransporter, isoform 2, (KCC2), which normally extrudes Cl^-. Interestingly, a reduction in KCC2 expression and/or function is involved in the pathogenesis of several neurological disorders, including epilepsy and neuropathic pain [9–15]. Motivated by the clinical relevance of hyperexcitability caused by changes in KCC2 activity, conductance-based compartmental models have been used to study how changes in E_{Cl} influence inhibitory control of neuronal spiking [5].

E_{Cl} can change as a result of altered KCC2 expression or activity [7,16,17]. E_{Cl} can also change dynamically, on a fast time scale, as a result of Cl^- flux through $GABA_A$ receptors, particularly in small structures like distal dendrites [2,4,18]. If E_{Cl} changed only slowly, it could be reasonably approximated as static relative to other neuronal processes occurring on a faster time scale; however, since E_{Cl} changes rapidly, it may interact in

Author Summary

Fast synaptic inhibition relies on chloride current to hyperpolarize the neuron or to prevent depolarization caused by concurrent excitatory input. Both scenarios necessarily involve chloride flux into the cell and, thus, a change in intracellular chloride concentration. The vast majority of models neglect changes in ion concentration despite experimental evidence that such changes occur and are not inconsequential. The importance of considering chloride homeostasis mechanisms is heightened by evidence that several neurological diseases are associated with deficient chloride extrusion capacity. Steady state chloride levels are altered in those disease states. Fast chloride dynamics are also likely affected, but those changes have yet to be explored. To this end, we built an electrodiffusion model that tracks changes in the concentration of chloride plus multiple other ion species. Simulations in this model revealed a multitude of complex, nonlinear interactions that have important consequences for the efficacy of synaptic inhibition. Several predictions from the model were tested and confirmed with chloride imaging experiments.

potentially complex ways with important neuronal processes like synaptic integration. To investigate those interactions, one must treat $[Cl^-]$ as a dynamical quantity evolving in space and time.

The spatio-temporal dynamics of $[Cl^-]_i$ depend on several factors, including $GABA_A$R-mediated Cl^- flux, longitudinal diffusion within dendrites and the soma, and CCC activity. Furthermore, Cl^- dynamics involve complex non-linear interactions with other ion species, which have been overlooked by previous models [19]. To understand how these dynamical processes interact with each other, we built an electrodiffusion model that monitors intra- and extracellular concentrations of several ion species (Cl^-, Na^+, K^+, Ca^{2+}, HCO_3^-, H^+, HPO_4^{2-}, $H_2PO_4^-$) across neuronal compartments (see Fig. 1A–C). Our model revealed several consequences of impaired Cl^- extrusion on neuronal function, including a positive feedback loop between intracellular Cl^- accumulation and excitatory activity or spiking that can lead to catastrophic failure of inhibition. Several predictions of the model were confirmed by direct measurement of $[Cl^-]_i$, by fluorescence lifetime imaging microscopy (FLIM).

Results

E_{Cl} and E_{GABA} depend non-linearly on KCC2 activity and synaptic input

Past experiments have established that Cl^- extrusion via KCC2 plays a crucial role in maintaining the values of E_{Cl} and E_{GABA} below the resting membrane potential [20], but they have not established how KCC2 activity relates quantitatively to E_{Cl} and E_{GABA}, in particular under conditions of ongoing, distributed synaptic input. Therefore, as a first step, we varied KCC2 activity and measured the impact on E_{Cl} and E_{GABA} (measured at the soma) in a model neuron receiving a fixed level of background excitatory and inhibitory synaptic input (Fig. 1D). Values of E_{Cl} and E_{GABA} in middle and distal dendrites are described by similar curves shifted to slightly more depolarized values (data not shown) consistent with the somato-dendritic gradient described below. This is important since neurons *in vivo* are bombarded by synaptic activity [21], but it remains unclear how this may affect E_{Cl} and, in turn, be affected by E_{Cl}. Consistent with qualitative experimental findings [9,22,23], both reversal potentials underwent depolarizing shifts as KCC2 activity was reduced, with E_{Cl} approaching the mean membrane potential (Fig. 1D). Notably, E_{GABA} was less negative than E_{Cl}, especially at high values of KCC2 activity, consistent with E_{GABA} depending jointly on $[Cl^-]_i$ and $[HCO_3^-]_i$ [24]. However, unlike the large depolarizing shift in E_{Cl} caused by reducing KCC2 activity, increasing KCC2 activity beyond its normal value caused only a marginal hyperpolarizing shift in E_{Cl}, which approached the K^+ reversal potential (E_K) near -90 mV. This is consistent with KCC2 normally operating near equilibrium. Hence, while reduction in KCC2 activity can cause strong reduction of inhibition, excess KCC2 activity has a limited influence on the strength of inhibition, insofar as we assume that strength of $GABA_A$R-mediated inhibition is a function of the value of E_{GABA}.

Thus, in addition to validating our model, this first set of simulations revealed an interesting nonlinear relationship between KCC2 activity and E_{Cl}. However, we expected that E_{Cl} should depend not only on KCC2, but also on factors like $GABA_A$R input – this was the main motivation for developing an electrodiffusion model. As a preliminary test, we varied the rate of inhibitory synaptic input together with KCC2 activity. Results show that E_{Cl} underwent a depolarizing shift, the magnitude of which depended on KCC2 activity, as the rate of inhibitory input increased (Fig. 1E). At a normal KCC2 level, increasing the activation rate of $GABA_A$R synapses from 0.2 to 5 Hz drove E_{Cl} up by only 7 mV, whereas the same change in activation rate drove E_{Cl} up by 24 mV when KCC2 activity was decreased to 33% of its normal value. Thus, KCC2 activity not only controls baseline E_{Cl}, it also determines how stably E_{Cl} is maintained when the Cl^- load is increased by synaptic input. Tonic inhibition due to activation of extrasynaptic $GABA_A$ receptors by ambient GABA can also contribute to intracellular Cl^- accumulation and depolarize E_{Cl}. To test the impact of tonic inhibition, we performed simulations with and without this form of inhibition. Results obtained with and without tonic inhibition were qualitatively the same (Fig. 1E).

To test experimentally the impact of the level of KCC2 activity on intracellular Cl^- accumulation, we loaded neurons in primary cultures (>21 days in vitro; DIV) with MQAE and measured changes in $[Cl^-]_i$ using FLIM. FLIM measurements have the advantage of being unbiased by the amount of indicator from cell to cell (Fig. 2A, B), minimizing the variability between measurements as well as shielding the measurements from changes in cell volumes [25]. We first bath applied the $GABA_A$R agonist muscimol to trigger Cl^- influx through $GABA_A$R channels. We then applied various concentrations of furosemide or VU 0240551 for 20 minutes to block KCC2 activity. In the presence of Cl^- load through activated $GABA_A$ channels, application of furosemide or VU 0240551 led to dose-dependent Cl^- accumulation (Fig. 2C, D), in agreement with the predictions of simulations (cf. Fig. 1D). At high doses, furosemide can antagonize both KCC2 and NKCC1; however, at > 21 DIV, hippocampal neurons in culture are generally thought to fully express KCC2 but to no longer express NKCC1 [6]. To test this, we used bumetanide at a concentration (50 μM) where it selectively blocks NKCC1. Administration of bumetanide to cells exposed to muscimol cause no change in $[Cl^-]_i$ (Fig. 2D). The presence of significant Cl^- export through KCC2 may however mask any NKCC1-mediated Cl^- import. To test for this, we blocked KCC2 with the recently developed selective blocker VU 0240551 [25]. Further addition of bumetanide after KCC2 blockade had no effect on $[Cl^-]_i$, confirming absence of significant NKCC1-mediated transport in these neurons (Fig. 2D). These results indicate **a)** significant KCC2 co-transport in > 21 DIV hippocampal neurons in culture, maintaining $[Cl^-]_i$ at a low level, and **b)** that both furosemide and

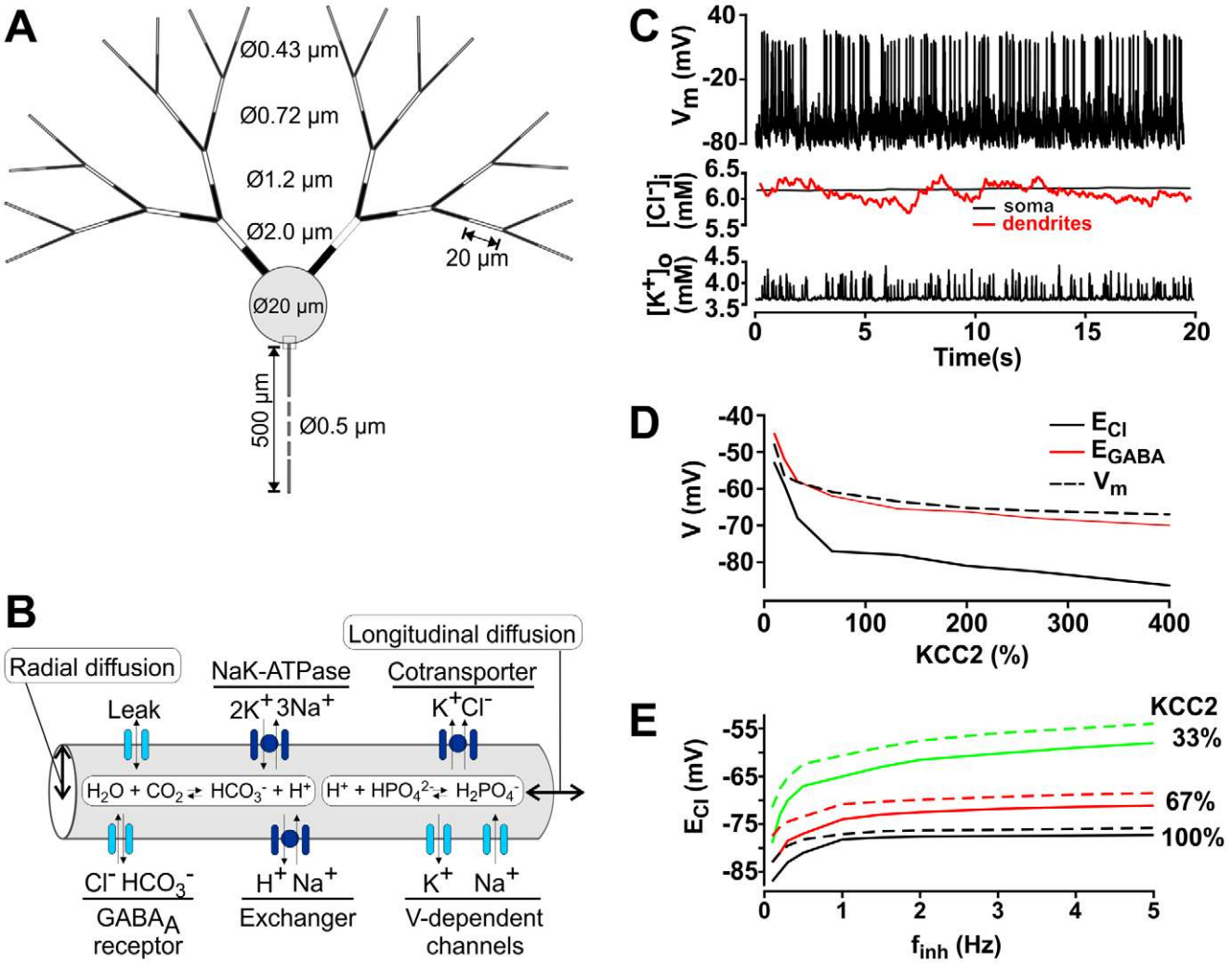

Figure 1. Summary and initial validation of model. A. Schematic of model neuron showing geometry and compartment dimensions. **B.** Summary of ion flux mechanisms included in the model (see Methods for details). Diffusion in the extracellular space is not depicted. **C.** Sample traces of membrane potential together with $[K^+]_o$ measured in the extracellular shell surrounding the soma and $[Cl^-]_i$ measured in the soma (black) and in a dendrite (red). This is only a subset of ion species whose concentrations were continuously monitored in all compartments, and from which reversal potentials were continuously updated. **D.** As predicted, reducing KCC2 below its "normal" level (100%) caused large depolarizing shifts in E_{Cl} and E_{GABA}, whereas increasing KCC2 up to 400% above normal caused only minor hyperpolarizing shifts. Simulation includes background synaptic input with f_{inh} = 0.8 Hz and f_{exc} = 0.2 Hz/synapse. The dashed line represents the mean value of membrane potential averaged over 200 s. **E.** Reversal potentials also depended on the rate of $GABA_AR$ input, which dictates the Cl^- load experienced by the neuron. Increasing f_{inh} caused a depolarizing shift in E_{Cl}, the extent of which increased when KCC2 was decreased. For these simulations, f_{inh}/f_{exc} ratio was fixed at 4 and f_{inh} was varied from 0.05 Hz to 4.8 Hz. Dashed lines represent results from simulations performed with tonic $GABA_A$ conductances while solid lines represent simulations performed without it.
doi:10.1371/journal.pcbi.1002149.g001

VU 0240551 could be used under these conditions to selectively block KCC2-mediated transport.

With the importance of nonlinear interaction between $GABA_AR$ activity and KCC2 activity for intracellular Cl^- regulation thus established, we moved onto more detailed analysis of how Cl^- flux impacts the efficacy of synaptic inhibition.

Transmembrane Cl^- gradient may vary between cellular compartments depending on the spatial distribution of synaptic input and cotransporter activity

Spatial variation in E_{Cl} (or E_{GABA}) between cellular compartments has been observed in several experiments [20,26–29] but it is not typically accounted for in conventional neuron models. While a longitudinal, axo-somato-dendritic $[Cl^-]_i$ gradient could be due to differentially distributed cotransporter activity, it could also arise from intense focal $GABA_AR$-mediated input. To test the latter scenario, we simulated high frequency $GABA_AR$-mediated input to a single dendritic synapse and measured $[Cl^-]_i$ at different distances from the synapse at different times after the onset of input (Fig. 3A). Under the conditions tested, a $GABA_AR$ synapse activated at 50 Hz produced a longitudinal $[Cl^-]_i$ gradient of 50 µM/µm, which extended as far as 60 µm and could yield changes in E_{GABA} on the order of 5 mV within 200 ms (Fig. 3A). There were only subtle differences between centripetal and centrifugal diffusion (*i.e.* toward or away from soma, respectively; Fig. 3B). According to these data, if a $GABA_A$ synapse receives sustained high frequency input, $[Cl^-]_i$ will increase near that synapse, influencing E_{GABA} at the original synapse as well at

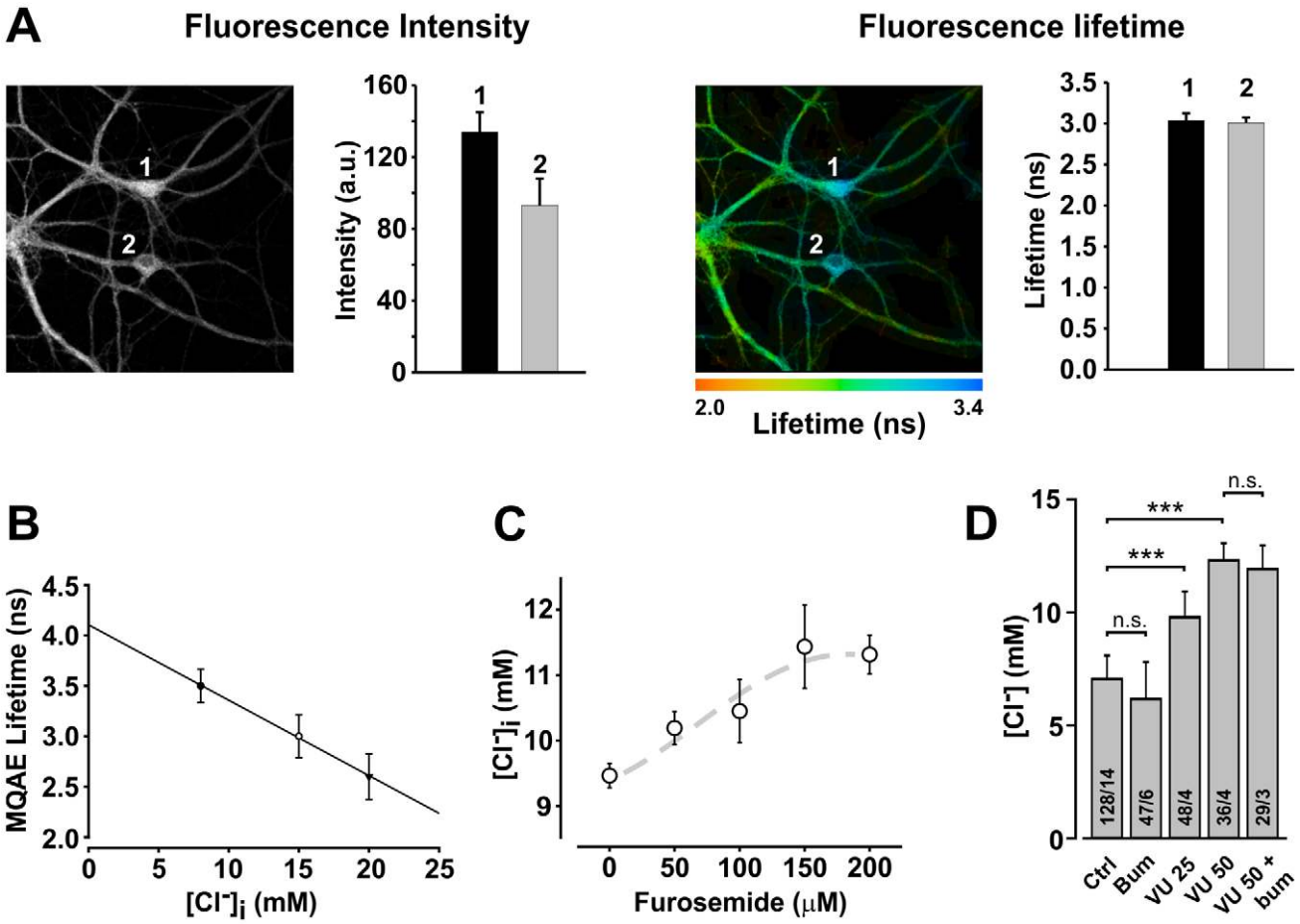

Figure 2. Measurements of $[Cl^-]_i$ in neurons with MQAE using Fluorescence Lifetime Imaging Microscopy (FLIM). A. Two-photon excitation fluorescence of MQAE-loaded hippocampal neurons (26 DIV). The mean intensity of MQAE fluorescence within the cell bodies 1 & 2 was significantly different (*left*), which could be interpreted as indicating different levels of $[Cl^-]_i$ or different dye uptake and accumulation between the two cells. The lifetime maps of the same cells are shown in the micrograph on the *right*. Note how, in contrast to intensities, the fluorescence lifetime of both cells were not significantly different indicating that there were no difference in $[Cl^-]_i$ between the two cells. Values are mean ± S.D. of all pixels in each cell body. **B.** Measurements of MQAE lifetime at different $[Cl^-]_i$ inside the cell body after membrane permeabilization and equilibration with $[Cl^-]_o$ at 8, 15 or 20 mM (N = 73 cells/12 coverslips). According to the Stern-Volmer equation: $\tau_0/\tau = 1 + Ksv[Cl^-]$. The measured Ksv from these data was 32 M^{-1}, consistent with previous reports [86]. **C**. Effect of increasing concentration of furosemide (to block KCC2) on $[Cl^-]_i$ in cultured neurons exposed to 100 μM muscimol (to evoke a constant Cl^- load by opening $GABA_AR$; N = 75 cells/10 coverslips). **D**. The selective KCC2 antagonist VU 0240551 caused a dose-dependent significant increase in $[Cl^-]_i$ ($p<0.05$), but bumetamide had no significant (n.s.) effect alone or after blocking KCC2 with VU 0240551, indicating lack of significant NKCC1 transport in these cells (N indicated in each bar = cells/coverslips; ***, $p < 0.001$).

doi:10.1371/journal.pcbi.1002149.g002

nearby synapses. This was further investigated by placing a "test" $GABA_A$ synapse (activated at 5 Hz) at varying distances from the original $GABA_A$ synapse (activated at 50 Hz). Both synapses were activated simultaneously. As predicted, E_{GABA} at the test synapse was affected by other $GABA_AR$-mediated input on the same dendrite as far away as 50 μm (Fig. 3C *top*), or even farther when KCC2 activity was reduced. However, interactions also depended on synapse position relative to the neuron topology; for instance, synapses in relatively close proximity but located on different primary dendrites exhibited little if any interaction (Fig. 3C *bottom*), consistent with the soma acting as a sink that clamps $[Cl^-]_i$.

Under *in vivo* conditions, neurons are known to be constantly bombarded by synaptic input [30]. We therefore tested whether this synaptic noise affects $[Cl^-]_i$ differently depending on the cellular compartment. We performed simulations in the presence or absence of KCC2 activity and in the presence or absence of synaptic noise. Simulations of distributed ongoing synaptic input with KCC2 distributed uniformly across the cell compartments yielded a clear somato-dendritic $[Cl^-]_i$ gradient (Fig. 4A *black*). In contrast, in the absence of simulated synaptic noise, there was no significant somato-dendritic $[Cl^-]_i$ gradient despite the presence of KCC2 (Fig. 4A *green*). Lack of a significant somato-dendritic $[Cl^-]_i$ gradient was also observed in the reverse scenario, i.e. in the presence of synaptic noise but without KCC2 (Fig. 4A *red*). Thus, a significant somato-dendritic $[Cl^-]_i$ gradient can exist when there is ongoing Cl^- influx, redistribution of that Cl^- load via diffusion, and Cl^- extrusion by KCC2. This clearly demonstrates that differential extrusion, i.e. inhomogeneous KCC2 density (see below), is not necessary for inhomogeneous transmembrane Cl^- gradients.

To test the predictions made by the model, we used FLIM to measure $[Cl^-]_i$ in MQAE-loaded neurons in culture (Fig. 4B). To mimic distributed Cl^- influx across the dendritic tree, we exposed the cultures to 100 μM muscimol. FLIM measurements indicated

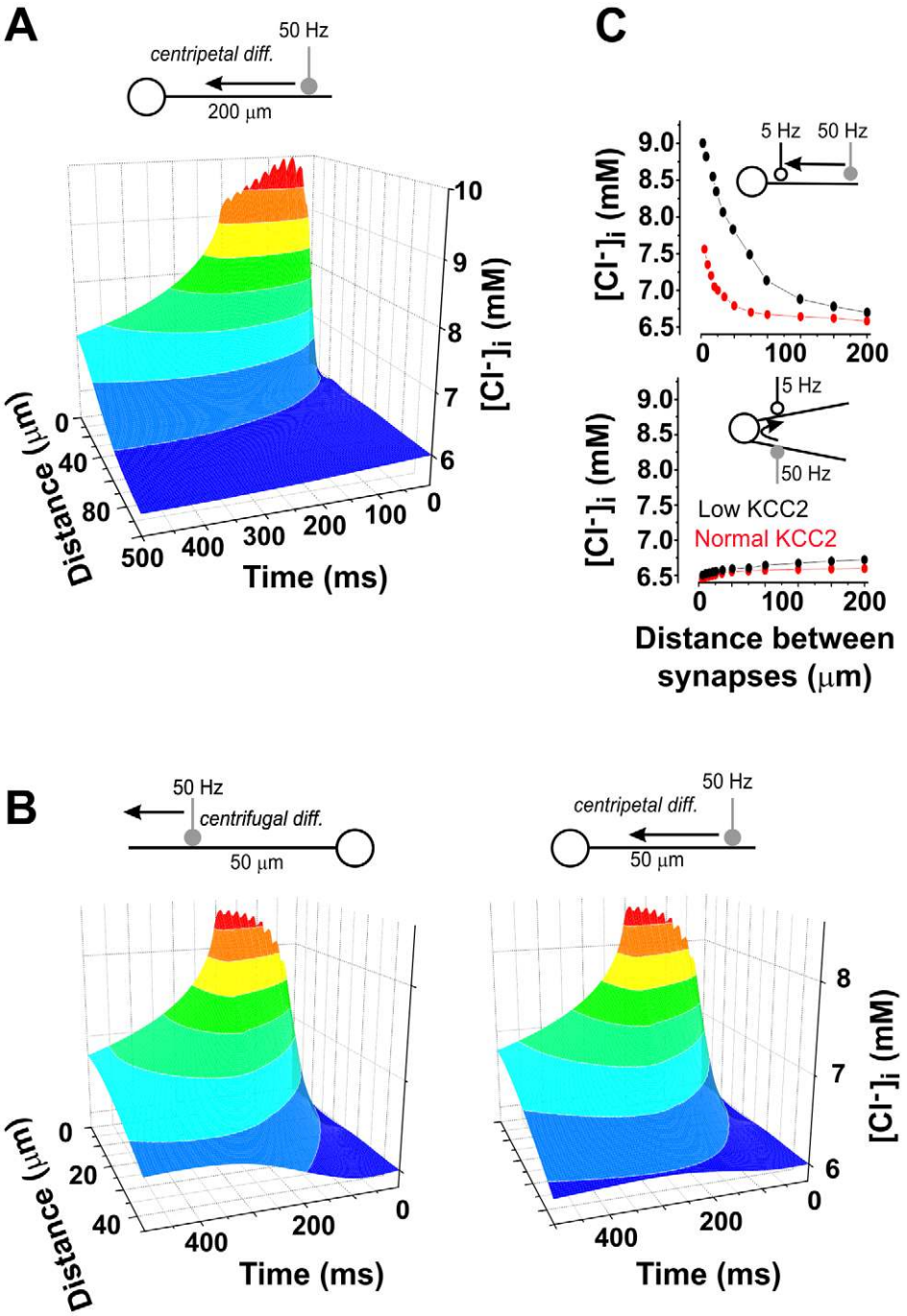

Figure 3. Redistribution of intracellular Cl^- through electrodiffusion. A. Chloride influx through a single $GABA_AR$ synapse (located at 200 μm from the soma) activated at 50 Hz produced a substantial longitudinal gradient in $[Cl^-]_i$ extending 60 μm on each side of the input. **B.** Chloride influx through a single $GABA_AR$ synapse (this time located at 50 μm from the soma) produced a longitudinal gradient which is steeper toward the soma (centripetal diffusion) than away from the soma (centrifugal diffusion). For this simulation, we used dendrites with constant diameters to ensure that the difference between left and right panels is due to the sink effect of the soma and not to the conical shape of the dendrite. We also lengthened the dendrite and increased the number of compartments to 60 compared to the cell geometry summarized in Fig. 1. **C.** Spread of Cl^- entering through one synapse (activated at 50 Hz) to a second "test" synapse (activated at 5 Hz) at varying inter-synapses distances was measured for normal and low (10%) KCC2 levels. Both synapses were activated simultaneously. For synapses positioned on the same primary dendrites (upper panel), the test synapse experienced a sizeable increase in $[Cl^-]_i$, especially when KCC2 was reduced, but there was no appreciable spread of Cl^- between synapses located on different primary dendrites (lower panel).
doi:10.1371/journal.pcbi.1002149.g003

a significant $[Cl^-]_i$ gradient along dendrites (Fig. 4B *top*) which was either reduced by bicuculline (Fig. 4B *middle* and 4C) or blocked by the addition of furosemide or the recently developed more specific KCC2 inhibitor VU 0240551 [25] (Fig. 4B *bottom* and 4C), consistent with predictions from simulations (cf. Fig. 4A). The small remaining gradient in the presence of furosemide may

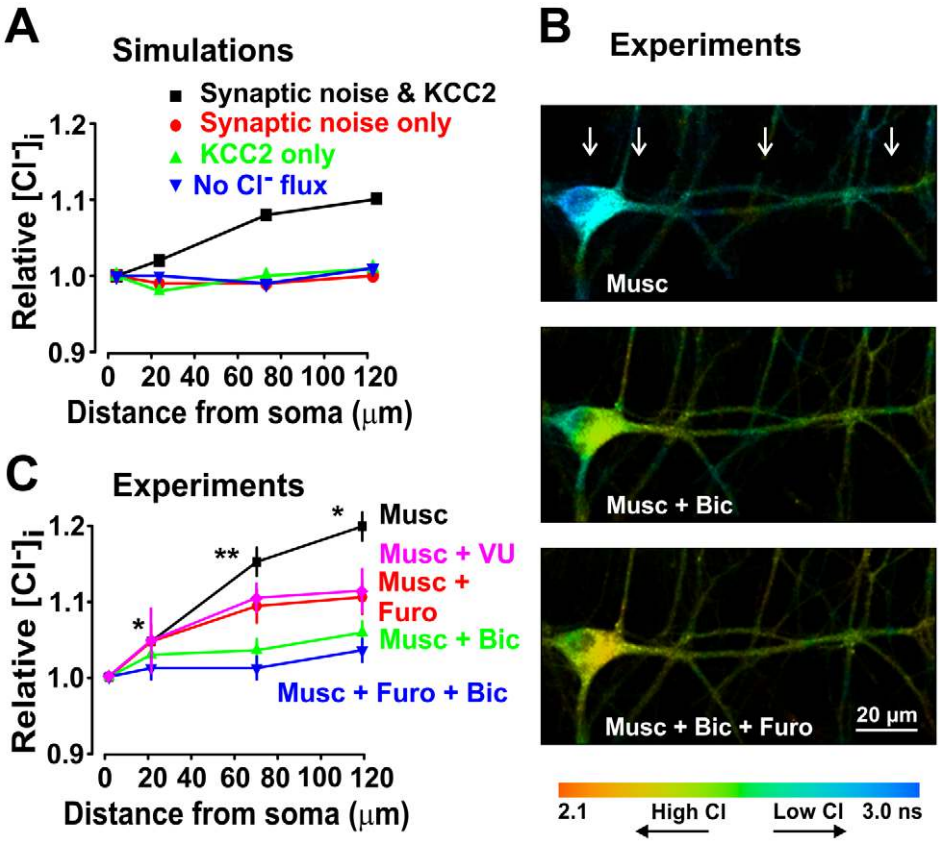

Figure 4. A standing somato-dendritic Cl^- gradient is caused by the joint action of KCC2 activity and $GABA_AR$ mediated synaptic input. A. Distribution of $[Cl^-]_i$ in a modeled dendrite as a function of distance from the soma in the presence and absence of Cl^- load due to distributed synaptic activity and of Cl^- extrusion through uniformly distributed KCC2. **B**. Photomicrographs of an example cell loaded with MQAE with lifetime color coding (blue: low Cl^- concentration, red: high Cl^- concentration). Intracellular Cl^- concentration was measured in the presence of muscimol (Musc; 100 μM) and/or bicuculline (Bic; 100 μM) and/or furosemide (Furo; 200 μM) and/or VU 0240551 (VU, 15 μM). Arrows indicate the location where measurements were performed. **C**. Effect of tonic activation of $GABA_ARs$ by muscimol on $[Cl^-]_i$ in real dendrites as a function of distance from the soma (each data point represent mean ± SEM taken from 10–12 neurons; values from several dendrites were averaged for each cell). Bicuculline and/or furosemide and/or VU 0240551 were added to block Cl^- loading and extrusion, respectively.
doi:10.1371/journal.pcbi.1002149.g004

indicate the presence of another chloride transport mechanism not accounted for in the model.

Our simulations were based on the assumption of even distribution of KCC2 along the dendrites and this configuration appears to be sufficient to explain the somato-dendritic gradient observed. However, this does not rule out the possibility of a gradient of KCC2 along the dendrites. To test for the presence or absence of such gradient, we sought to perform quantitative fluorescence immunocytochemical analysis of the distribution of KCC2 along dendrites. Measuring KCC2 immunolabeling may not be sufficient, however, to obtain an estimate of the distribution of functional KCC2 because it has recently been suggested that the oligomeric form of KCC2 is the functional one [31,32]. To specifically measure the density of KCC2 dimers along the dendrites we took advantage of a technique we recently developed, entitled Spatial Intensity Distribution Analysis (SpIDA) which allows quantitative measurement of the density and oligomerization of proteins from conventional laser scanning confocal microscopy analysis of immunocytochemical labeling [33,34]. We thus applied SpIDA to analysis of of KCC2 immunostaining of dendrites of the neurons used in the pharmacological experiments described above (Fig. 4). The monomeric quantal brightness was estimated using immunolabeling of KCC2 in neurons that have been in culture for only 5 days, because, at that stage of development, KCC2 has been shown to be essentially monomeric [31]. The monomeric quantal brightness was estimated to be $3.9\times10^6\pm0.2$ (mean ± SEM) intensity units or 3.9±0.2 Miu, and was constant along the dendrite of 5-DIV neurons (52 regions from 11 neurons). Using automated intensity binary masks [35], the dendrites of the mature neurons (> 21 DIV) were carefully detected and intensity histograms were generated for each analyzed region and a two-population (monomers and dimers) mixture model was assumed. For each analyzed region, SpIDA was performed on the image of the z-stack (0.5 μm between images) that had the brightest mean intensity in the chosen region. To estimate the true membrane density of KCC2, the final value for each region was averaged over the two adjacent images of the z-stack. A neuron with example regions and their corresponding histogram and SpIDA fit values are presented in Figure 5A,B. The results indicate that the membrane density of KCC2 is constant along the dendrites, at least as far as 200 μm from the center of the cell body (Fig. 5C).

While our experimental results indicate homogeneous distribution along the dendrite length, this does not necessarily apply to all conditions and, in particular, our analysis did not focus on local inhomogeneities, e.g. microdomains. We therefore also sought to determine if longitudinal intracellular Cl^- gradients could also arise from inhomogenous CCC activity at small length scales. For instance, non-uniform distribution of KCC2 at the subcompartent-level might produce local gradients comparable to those

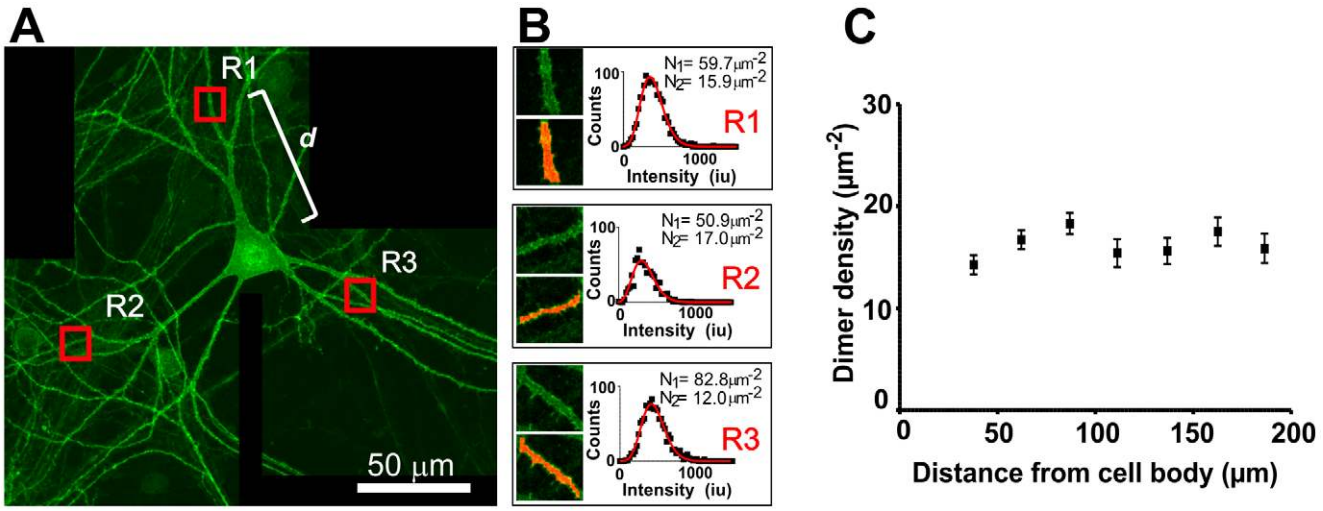

Figure 5. The density of KCC2 is constant along dendrites of neurons in culture. A. Three confocal images tiled showing a neuron immunostained with a fluorescent anti-KCC2 antibody Images are of size 1024×1024pixels with a pixel size of 0.115 μm and a 9.1 μs pixel dwell time. Three red squares representing example regions analyzed are shown, in **B**, with their corresponding binary mask used to delineate the labeled dendrite. The intensity histograms of the representative subregions delimited in **A** are shown in **B** with their corresponding SpIDA fit and recovered values of monomer (N_1) and dimer (N_2) densities. The distance (e.g., *d* in **A**) between the center of the cell body and the center of the analyzed region was also measured. **C**. Graph of the density of KCC2 dimers at the dendrite surface as a function of the distance from the cell body obtained with SpIDA. 823 regions were analyzed from 27 neurons. Error bars show SEM.
doi:10.1371/journal.pcbi.1002149.g005

observed with synaptic inputs (see Fig. 3). Indeed, clustering of KCC2 has been observed near some synapses [36], but KCC2 near excitatory synapses has been shown to serve a role in scaffolding rather than as a co-transporter [37]. Nevertheless, to test whether subcellular distribution of KCC2 can yield local gradients, we simulated high frequency synapses at 20 μm intervals, between each firing synapses Cl^- extrusion through KCC2 was localized at a single point that was placed at different distances from the synapses (Fig. 6A). In all cases, the location of KCC2 had an impact on E_{Cl} of <2 mV. Thus, our simulations showed that subcompartemental distribution of KCC2 (i.e. inhomogeneities on the spatial scale of 0-10 μm) has little impact on the perisynaptic value of E_{Cl}.

The results above do not rule out the possibility of inhomogeneities in CCC expression underlying gradients in other cells types, as well as inhomogeneities in the axon initial segment and soma with respect to dendrites. For instance, absence of KCC2 in the axon initial segment (AIS) [9,38], selective expression of the inward Cl^- transporter NKCC1 in the AIS [28], or the combination of both expression patterns would be expected to cause E_{Cl} to be less negative in the AIS. To test E_{Cl} in the AIS and how it impacts neighboring compartment, we simulated different levels of NKCC1 in the AIS in combination with different levels of KCC2 in the soma and dendrites with or without background synaptic input (Fig. 6B–C). NKCC1 expression in the AIS can produce an axo-somatic $[Cl^-]_i$ gradient, but this gradient does not extend far, if at all, into the dendrites (Fig. 6B). As expected, combining NKCC1 expression in the AIS with synaptic noise (like in Fig. 4A) resulted in a "double gradient" (Fig. 6C *right panel*).

Thus, simulations in our electrodiffusion model demonstrated that subcellular distribution of $GABA_AR$ input and CCC activity can produce spatial inhomogeneities in E_{Cl}, which should translate into inhibitory input having differing efficacy depending on the location of the synapse. This is true even if KCC2 activity is uniformly distributed in the presence of background $GABA_AR$ input. Moreover, focal Cl^- influx through one synapse (or a cluster of synapses) can affect the efficacy of neighbouring synapses, although this depends on subcellular localization of those interacting synapses, *e.g.* proximity to the soma. In contrast, subcompartmental inhomogeneity in KCC2 activity is not sufficient to cause local $[Cl^-]_i$ gradients.

Diffusion and KCC2 activity determine how robustly the transmembrane chloride gradient is maintained during high frequency synaptic input

Figures 4 and 6 emphasized how spatial variations in $[Cl^-]_i$ can arise from ongoing $GABA_AR$ input. To extend these results to include temporal changes in E_{Cl}, we considered how $[Cl^-]_i$ evolves during stimulus transients. This was motivated by experimental observations that E_{GABA} can rapidly collapse during bursts of $GABA_AR$ synaptic events [20,28,39,40]. Activity-dependent changes in E_{GABA} depend on the location of the input: somatic input has less impact on E_{GABA} than dendritic input [4,28]. Simulations in our electrodiffusion model replicated those experimental data (Fig. 7A) as well as results from simpler models [19]. A train of synaptic inputs to the soma produced a small depolarizing shift in E_{GABA}, which translated into a small reduction in $GABA_AR$-mediated current. The depolarizing shift in E_{GABA} was greater and occurred increasingly faster for input to progressively more distal dendrites. This was despite the presence of KCC2 (*red*). Removing KCC2 (*black*) increased the amplitude and speed of the collapse in Cl^- gradient during high frequency input to distal dendrites, but had virtually no impact for input to the soma. The finding that amplitude of the initial synaptic event in each of the compartments was unaffected by removing KCC2 appears to contradict the observation that the standing $[Cl^-]_i$ gradient depends on KCC2 activity (see Fig. 4). We hypothesized that this was due to the absence of ongoing Cl^- load caused by the lack of background synaptic activity. We therefore repeated simulations shown in Figure 7A but with background synaptic input (Fig. 7B). As predicted, the initial IPSC amplitude was affected by the KCC2 activity level when background synaptic input was present (compare Fig. 7B and A). These results suggest

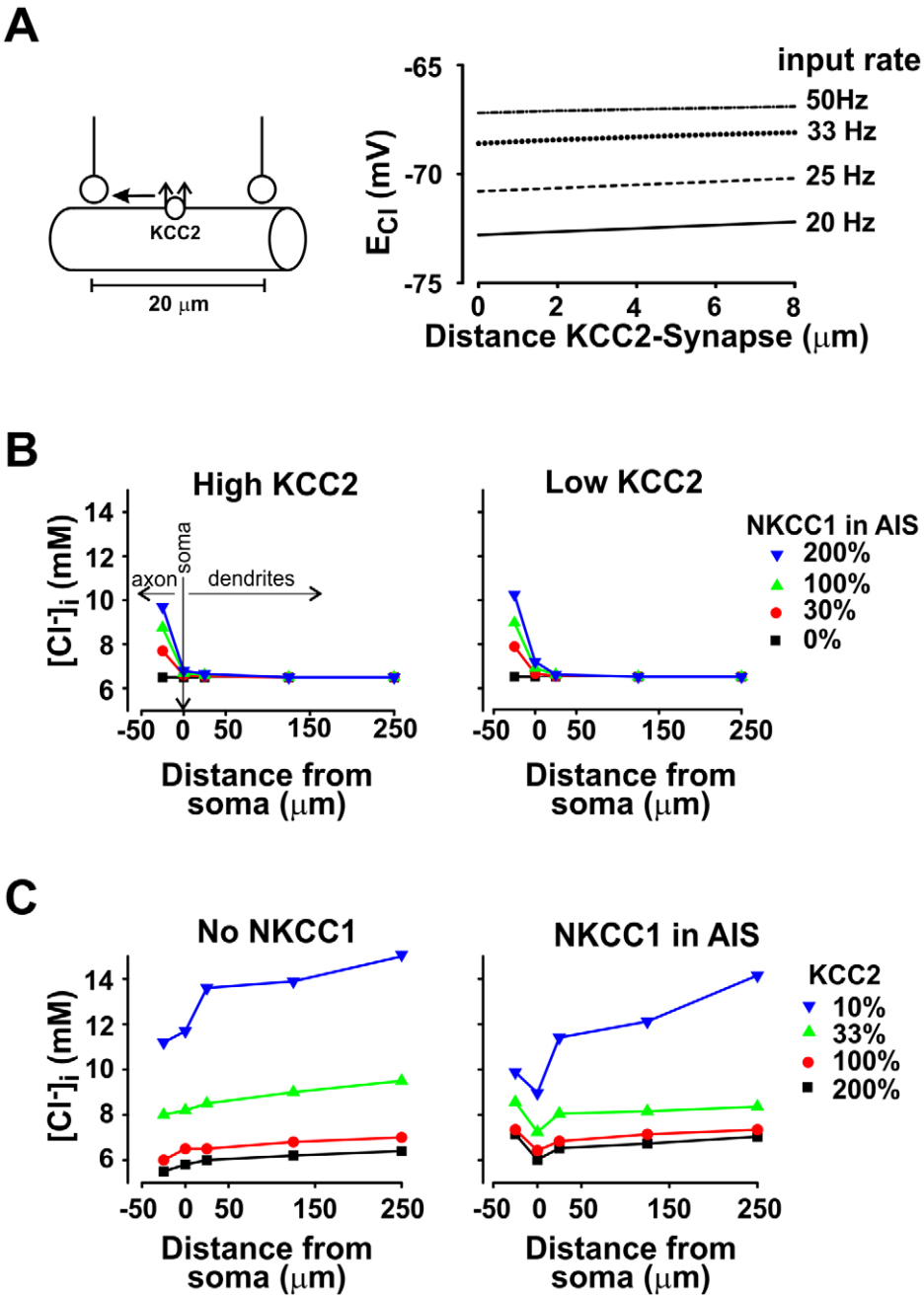

Figure 6. Inhomogenous CCC distribution can create large-scale, but not fine-scale, intracellular $[Cl^-]_i$ gradients. A. *left*: To investigate whether the perisynaptic distribution of KCC2 can produce fine-scale intracellular $[Cl^-]_i$ gradients, we varied the subcompartmental distribution of KCC2 by concentrating it in a single location in each compartment at varying distances from a bursting synapse. We divided the compartment into 20 1-μm-long sections. Total amount of KCC2 per compartment was constant at 100%. Inhibitory synapses were located at 20 μm from each other and were activated at high frequency. *Right*: Results show that the subcompartmental distribution has little impact on the perisynaptic value of $E_{Cl,}$ which contrasts with the impact of high frequency synaptic input (see Fig. 3) but is consistent with diffusion being responsible for rapid redistribution of intracellular Cl^- load. **B.** In the absence of synaptic activity, we inserted different levels of NKCC1 activity in the axon initial segment (AIS) and monitored the axo-somato-dentritic $[Cl^-]_i$ gradient for high (100%) and low (33%) levels of KCC2 activity (uniformly distributed, except in the AIS). Soma corresponds to 0 on *x*-axis; positive distance extends towards dendrites and negative distance extends towards axon, as summarized on left panel. **C.** In the presence of background synaptic activity (f_{inh} = 0.4 Hz; f_{exc} = 0.1 Hz) we simulated different levels of KCC2 activity (uniformly distributed, except in the AIS) and monitored the axo-somato-dentritic $[Cl^-]_i$ gradient in the presence (100%) or absence of NKCC1 in the AIS.
doi:10.1371/journal.pcbi.1002149.g006

that the rate of local intracellular Cl^- accumulation depends principally on diffusion (which redistributes the intracellular Cl^- load), whereas the extent of accumulation depends on KCC2 activity (which reduces intracellular Cl^- load via extrusion).

To investigate these processes more thoroughly, we systematically varied the intraburst frequency, location of the "test" synapse and KCC2 activity, and we measured the mean IPSC amplitude at the "test" synapse throughout the burst. During high

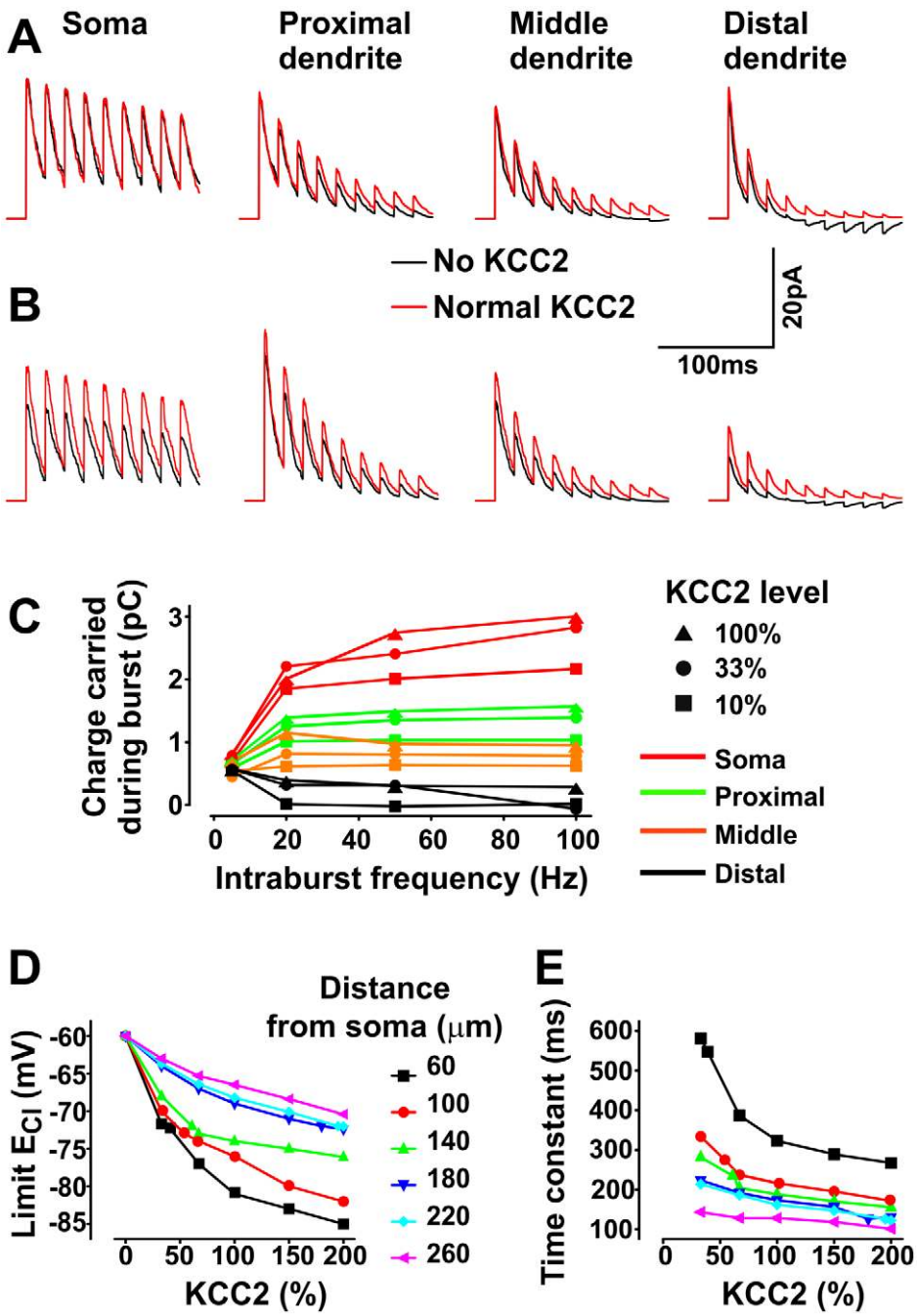

Figure 7. Dependency of Cl^- accumulation on the site of synaptic input and KCC2 level. Trains (40 Hz) of inhibitory postsynaptic currents (IPSCs) at a synapse located at one of four positions: soma and proximal, middle, and distal dendrites (40, 100, and 240 μm from soma, respectively) in simulations without (**A**) and with (**B**) background synaptic input (f_{inh} = 0.4 Hz, f_{exc} = 0.1 Hz). For this set of simulations, a single dendrite was lengthened (and number of compartments increased to 60) relative to the cell geometry summarized in Fig. 1A. Inversion of the IPSC was evident in the distal dendrites under conditions without KCC2 (*right panels*). **C**. Mean intraburst IPSC became smaller (*i.e.* less hyperpolarizing) with increasing distance from the soma and with decreasing KCC2 level. Synaptic background activity was the same as in **B**. Mean IPSC was measured at a "test" synapse activated at 40 Hz for 200 ms every second over 50 s of simulated time. Steady state value of E_{Cl} (**D**) and rate at which E_{Cl} approaches steady state (**E**) for different KCC2 levels and distances of "test" synapse from the soma. Steady state E_{Cl} reported in **D** was measured as the value to which E_{Cl} converged when $GABA_AR$ at the test synapse were artificially held open. This convergence was fit with a single exponential to determine the time constant reported in **E**.
doi:10.1371/journal.pcbi.1002149.g007

frequency input to distal dendrites, the net mean current through $GABA_AR$ synapses switched from outward to inward whereas the same rate of input to the soma continued to produce strong outward currents (Fig. 7C). Thus, while increasing intraburst frequency can effectively enhance hyperpolarization in the soma, it rapidly becomes ineffective in dendrites and can even become depolarizing in distal dendrites. For a fixed intraburst frequency, E_{Cl} converged to different steady-state levels (Fig. 7D) with

different rates (Fig. 7E) depending on the location of the test synapse and the level of KCC2 activity. In other words, the steady-state value of $[Cl^-]_i$ increased with distance from the soma (reminiscent of the standing gradient reported in Fig. 4A and C) and it decreased when KCC2 activity was increased. On the other hand, Cl^- accumulation converged to a steady state more rapidly with increased KCC2 activity as well as with distance from the soma. The two convergence processes are due to different phenomena: Enhanced KCC2 activity allows the dendrite to restrict the extent of Cl^- accumulation (see above), while Cl^- accumulates faster in distal dendrites simply because the effective volume is smaller and diffusion is restricted. In summary, under dynamic conditions, restricted diffusion in distal dendrites causes a rapid collapse of E_{GABA}, but the extent of this collapse is limited by KCC2, consistent with experimental measurements [8,9,28].

In dendrites, distributed $GABA_AR$ input mediates greater inhibition than higher frequency focal input

The above results led us to predict that, for equivalent total synaptic input, many broadly distributed $GABA_AR$ synapses activated at low frequency would produce greater hyperpolarization than a few clustered synapses (or just one synapse) activated at higher frequency, especially for synapses located on distal dendrites. We tested this by comparing the outward current produced by one synapse activated at an intraburst frequency of 50 Hz with the total hyperpolarizing current produced by ten distributed synapses activated at 5 Hz; this was repeated for dendritically and somatically positioned synapses (Fig. 8A). In the soma, ten synapses activated at 5 Hz produced more outward current than one synapse activated at 50 Hz (Fig. 8A *middle*). This is due to the fact that the total synaptic conductance does not scale linearly with frequency because of saturation. Even more important is the fact that distributed dendritic input is capable of producing a strong outward current despite Cl^- accumulation, whereas clustered dendritic input was totally inefficient in producing an outward current. These results suggest that dendritic inhibition is most effective when spatially distributed, consistent with data in Figs. 3 and 6. Maintaining spatially distributed $GABA_A$ synapses in dendrites is also important because the rapid dynamic collapse of distal hyperpolarizing $GABA_AR$ currents will limit their effectiveness at controlling somatic signals because membrane potential changes extend farther than changes in conductance [8,41]. Given that shunting remains even when E_{Cl} collapses, we submitted the neuron to distributed excitatory input and measured the mean firing frequency of the model neuron to verify that loss of hyperpolarizing current translates into effective disinhibition (Fig. 8A *right*). We found that firing rate reduction mirrored the change in charge carried (cf. Fig. 8A *right* and *middle* panels).

Enhancing $GABA_AR$ input may fail to enhance inhibition under conditions of impaired chloride homeostasis

In addition to synapse location, the rate and duration of synaptic inputs would be expected to interact with dynamic changes in E_{GABA} to alter the efficacy of inhibition. Although increasing the rate or duration of $GABA_AR$ inputs may initially increase IPSC amplitude, such changes would also accelerate depletion of the Cl^- gradient and thereby eventually reduce IPSC amplitude, at least when Cl^- influx overwhelms local diffusion mechanisms and Cl^- extrusion capacity. Using our model, we studied the influence of KCC2 activity level, synaptic frequency and time constant of $GABA_AR$-mediated events (τ_{IPSC}) on the mean current through a dendritic $GABA_AR$ synapse. Simulations indicated that increasing KCC2 activity always led to larger mean outward current. In contrast, increasing synaptic input frequency (Fig. 8B *left*) or τ_{IPSC} (Fig. 8B *right*) did not necessarily increase the mean current; in both cases, the mean current was largest at intermediate values of those parameters. Similarly, mean firing rate was reduced most at intermediate values of those parameters (Fig. 8C). To establish the generality and robustness of the result, we repeated simulations for neurons endowed with different ion channels affecting spike generation. We added non-inactivating Ca^{2+}-activated K^+ channels known to decrease firing rate or persistent Na^+ channels known to increase firing rate, and we also performed simulations in which dendritic Hodgkin-Huxley (HH) channels were concentrated at branch points. Although these modifications to the model changed the overall firing rate, our qualitative finding remained unchanged; that is, firing rate increased if $GABA_AR$ input was augmented beyond a certain level (Fig. 8C *right*).

The above results indicate that more or longer $GABA_AR$ inputs may not always produce more inhibition, *i.e.* stronger outward current. We therefore asked what $GABA_AR$ input conditions produce the strongest inhibition? This question was addressed by measuring which parameter combinations produced the largest outward current. We found that the $GABA_AR$ input frequency yielding the largest outward current increased with KCC2 activity and decreased with τ_{IPSC} (Fig. 8D). This optimal frequency was as low as 6 Hz when KCC2 activity was depleted to 10% of its normal value and τ_{IPSC} was set to 50 ms; in other words, $GABA_AR$-mediated synaptic events occurring either at lower or at higher frequencies than 6 Hz produced less outward current. The optimal $GABA_AR$ input frequency climbed to 28 Hz when KCC2 activity was set to baseline and τ_{IPSC} was set to 10 ms. Thus, the optimal $GABA_AR$ input frequency may vary quite widely depending on other factors, but the key observation is that beyond some point (determined by the robustness of Cl^- homeostasis), more $GABA_AR$ input does not necessarily produce more inhibition. Increasing the frequency of $GABA_AR$ input showed a similar inverted bell-shaped curve when estimating effective inhibition with either total charge carried or firing rate reduction (Fig. 8B and C).

Net current through $GABA_AR$ depends on the balance of chloride and bicarbonate flux

Results of simulations presented in Figure 7 showed that the current through $GABA_AR$ could reverse polarity if there was sufficient accumulation of intracellular Cl^-. However, as the Cl^- gradient collapses, one would expect Cl^- flux to stop, but not to change its direction; likewise, the IPSCs would be expected to become smaller but not to invert. Indeed, if the $GABA_AR$ is modeled as passing only Cl^- ions, the IPSC decreases in size as Cl^- accumulates intracellularly, but it does not reverse direction (Fig. 9A) thus showing that bicarbonate flux must be accounted for in order to explain IPSC inversion [42,43]. An important and novel feature of our model is that HCO_3^- is not assumed to be constant. Even if the relative stability of $[HCO_3^-]_i$ has been shown to result from complex interaction between HCO_3^- efflux, carbonic anhydrase-mediated reaction and proton extrusion mechanisms, most models choose to consider it constant *de facto*. However, simulating the various mechanisms involved in $[HCO_3^-]_i$ management proved a useful tool for investigating the legitimacy of assuming $[HCO_3^-]_i$ is constant and for studying potential interactions between Cl^- and HCO_3^- dynamics. Bicarbonate efflux produces an inward current, but that current is (normally) masked by the larger outward current produced by Cl^- influx, since the permeability ratio between Cl^- and HCO_3^- anions is approximately 4:1 [2,43]. But as the Cl^--mediated outward current becomes smaller, the HCO_3^--mediated inward

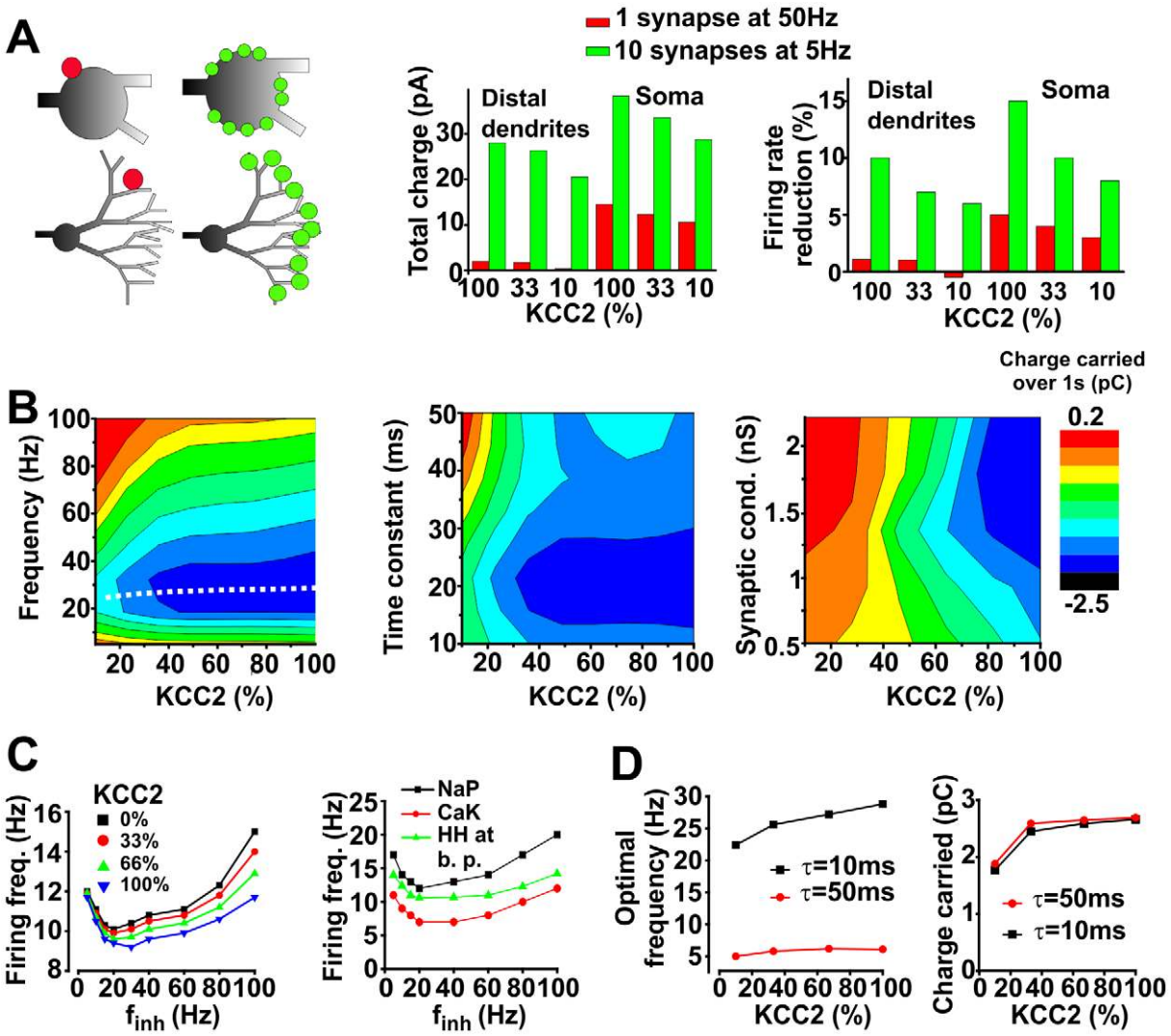

Figure 8. Efficacy of inhibition depends on spatial and temporal features of $GABA_AR$ input. A. Schematic shows synapse positioning (*left panel*). $GABA_AR$ input clustered at a single synapse (*red*) produced less outward current than the same total input distributed across ten spatially separated synapses (*green*), especially for input to the distal dendrites (*center panel*). To ensure that "total charge" translates into functionally relevant inhibition (*i.e.* reduction in spiking), we submitted the model to distributed excitatory input (f_{exc} = 0.2 Hz) and measured firing rate. As expected, reduction in firing frequency was greater when inhibitory input was spatially distributed (*right panel*). **B.** Net charge carried through a "test" synapse (*color*) consistently decreased as KCC2 activity was reduced, but increasing the frequency (*left panel*), time constant (*middle panel*) or conductance (*right panel*) of input at that synapse did not necessarily increase current amplitude. For the *left panel*, the time constant was held at 10 ms while the input frequency and KCC2 level were varied; the dotted line shows optimal frequency, which is re-plotted in **D**. For the *middle panel*, the input frequency was held at 30 Hz while the time constant and KCC2 level were varied. For the *right panel* input frequency and time constant were held at 30 Hz and 10 ms respectively while the conductance and KCC2 level were varied. Background synaptic activity was included in these simulations (f_{inh} = 0.4 Hz, f_{exc} = 0.1 Hz). Test synapse was positioned at 50 μm from the soma. **C**. We performed simulations similar to that in **B** but added distributed excitatory input to assess inhibition on the basis of firing rate reduction rather than on the basis of total charge (*left panel*). The pattern of inverted bell-shaped curves is consistent with **B**, thus confirming a net change in inhibition at the whole cell level. The graph on the *right* illustrates results obtained from simulations with models including Ca^{2+}-activated K^+ channels or persistent Na^+ channels. We also concentrated dendritic HH channels at branch points while preserving the total conductance of these channels. Results were qualitatively the same as in the graph on the *left*. **D.** Optimal input frequency depending on KCC2 level and time constant (*left panel*) and the corresponding current (*right panel*). Black curves correspond to dotted line on left panel of **B**. Note that this is the optimal frequency for activation of a single "test" synapse; optimal input frequency would necessarily decrease as the number of activated synapses increased, although the exact relationship would depend on the spatial distribution of those active synapses (see **A**) as well as the level of background synaptic activity.
doi:10.1371/journal.pcbi.1002149.g008

current becomes *relatively* larger, eventually causing the net current through $GABA_AR$ to become inward. Unlike the Cl^- gradient, the HCO_3^- gradient tends not to collapse (Fig. 9B) because intracellular HCO_3^- is replenished by carbonic anhydrase-catalyzed conversion of CO_2, which can readily diffuse across the membrane [44,45].

But although the reactants of the carbonic anhydrase-catalyzed reaction (*i.e.* CO_2 and H_2O) are not depleted, the forward reaction produces H^+ in addition to HCO_3^-. By removing HCO_3^-, $GABA_AR$ activity would be expected to reduce the intracellular pH, which has been observed experimentally [24]. Since accumulation of intracellular H^+ shifts the equilibrium point of

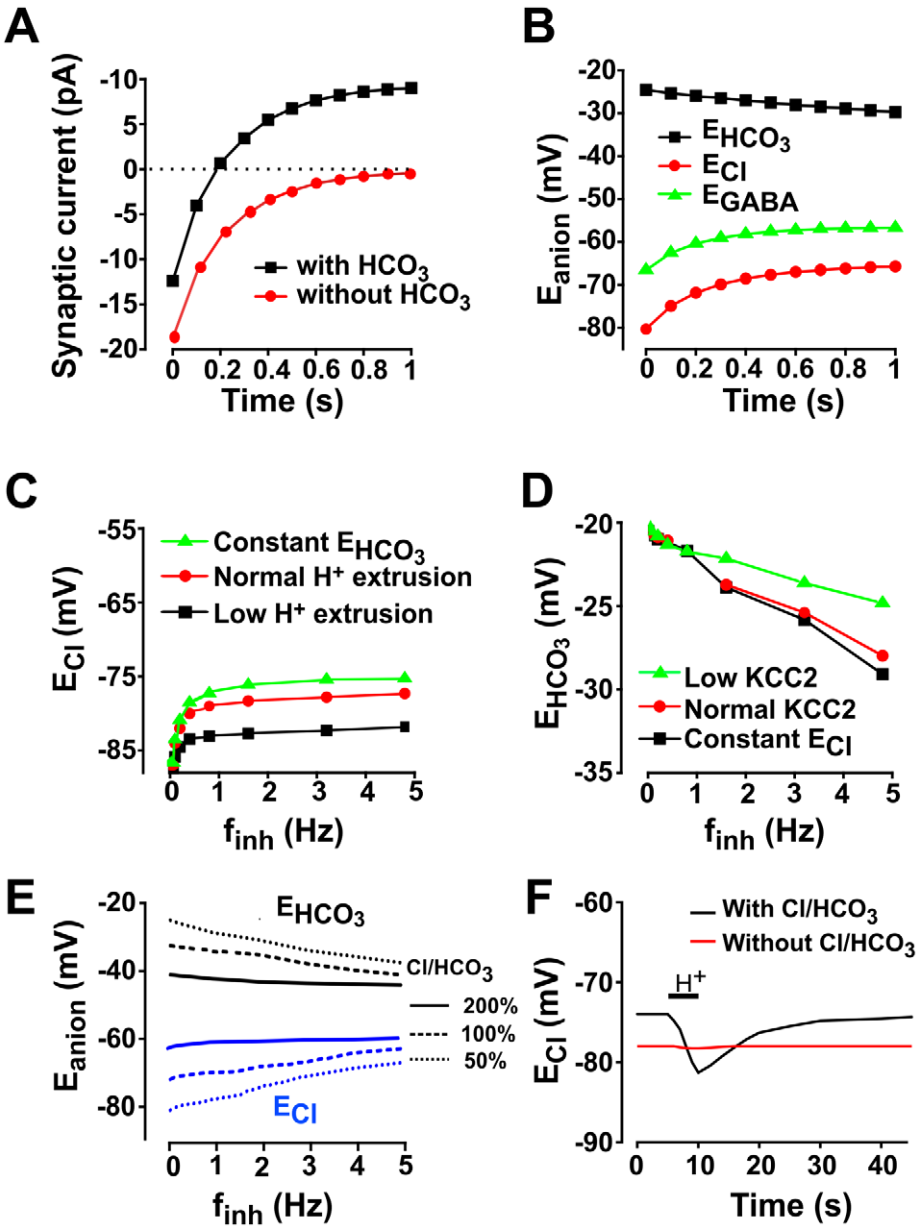

Figure 9. Trade-off between robustness of HCO_3^- and Cl^- homeostasis. A. Change in synaptic current over time as $GABA_AR$ synapse is held open. Notice in the standard model (*black*) that current eventually inverted; in contrast, current decayed to zero but did not invert in the model without HCO_3^- efflux (*red*). **B.** Change in reversal potentials over time for standard model and same test conditions as in **A**. Although small compared to changes in E_{Cl}, E_{HCO3} did shift (in the opposite direction). The balance of those changes determines the net shift in E_{GABA}, which explains the functional implications of predictions tested in **C** and **D** – a reduced change in E_{HCO3} should produce an enhanced change in E_{Cl}, whereas a reduced change in E_{Cl} should produce an enhanced change in E_{HCO3}. **C.** Encouraging HCO_3^- efflux through $GABA_AR$ by holding $[HCO_3^-]$ constant (*green*) exacerbated the depolarizing shift in E_{Cl}. Discouraging HCO_3^- efflux by reducing H^+ extrusion to 33% of normal (black), which in turn discourages the forward reaction catalyzed by carbonic anhydrase and accelerates depletion of intracellular HCO_3^-, mitigated the depolarizing shift in E_{Cl}. **D.** Conversely, encouraging Cl^- influx through $GABA_AR$ by holding $[Cl^-]$ constant (*black*) exacerbated the hyperpolarizing shift in E_{HCO3}. Discouraging Cl^- influx by reducing KCC2 activity to 10% of normal (green) mitigated the hyperpolarizing shift in E_{HCO3}. Effects in **C** were stronger than those in **D**, which illustrates how inter-relationships can be asymmetrical, *i.e.* pH regulation has a stronger impact on $[Cl^-]$ dynamics than Cl^- regulation has on pH dynamics under the conditions simulated here. **E.** Simulations similar to the ones conducted in **C** and **D** were performed but with the addition of Cl^-/HCO_3^- exchanger at different levels of activity. **F.** We performed a simulation in which we added an artificial H^+ influx for 5 s (horizontal bar). The proton influx caused a sizeable drop in $[HCO_3^-]_i$, thereby producing a hyperpolarizing shift in E_{HCO3}; that shift is greater in the model without the Cl^-/HCO_3^- exchanger (not shown). The resulting change in HCO_3^- gradient caused an inversion of Cl^-/HCO_3^- exchange that led to a significant lowering of E_{Cl}; this did not occur in the absence of the Cl^-/HCO_3^- exchanger.
doi:10.1371/journal.pcbi.1002149.g009

the reaction, intracellular HCO_3^- slowly decreases, with a time constant in the order of several seconds, which explains the small hyperpolarizing shift in E_{HCO3} seen in Figure 9B over long time scales. By E_{Cl} and E_{HCO3} shifting in opposite directions, E_{GABA} tends toward the membrane potential. We therefore predicted that reducing changes in E_{HCO3} would lead to greater changes in E_{Cl}

and, vice versa, that reducing changes in E_{Cl} would lead to greater changes in E_{HCO3}. To test the first prediction, $[HCO_3^-]_i$ was held constant (thus maintaining HCO_3^- efflux), which enhanced the depolarizing shift in E_{Cl}; on the other hand, increasing intracellular HCO_3^- depletion by reducing proton extrusion via the Na^--H^+ exchanger (thus reducing HCO_3^- efflux) mitigated the depolarizing shift in E_{Cl} (Fig. 9C). To test the second prediction, $[Cl^-]_i$ was held artificially constant, which enhanced the hyperpolarizing shift in E_{HCO3}; conversely, increasing intracellular Cl^- accumulation by reducing Cl^- extrusion via KCC2 mitigated the hyperpolarizing shift in E_{HCO3} (Fig. 9D). These results demonstrate a trade-off between stability of $[Cl^-]_i$ and stability of intracellular pH based on their common reliance on $[HCO_3^-]_i$. It remains an open question whether $[Cl^-]_i$ or intracellular pH is more strongly regulated under normal conditions, but one can reasonably extrapolate when KCC2 activity is reduced, that the primary depolarizing shift in E_{Cl} will conspire with a smaller secondary hyperpolarizing shift in E_{HCO3} to produce a large depolarizing shift in E_{GABA}. This is particularly relevant to steady state conditions because, on the time scale of individual synaptic events, pH buffering mechanisms are not saturated, while on longer time scales, the rate limiting components of HCO_3^- homeostasis are the slower kinetics of the HCO_3^- and H^+ membrane transporters.

The Cl^-/HCO_3^- exchanger can also play a role in pH management and Cl^- homeostasis regulation. To gain some insight into the impact of this exchanger, we repeated simulations of Figure 9C–D adding different levels of Cl^-/HCO_3^- exchanger activity to the model. As is the case for such ion exchangers, the Cl^-/HCO_3^- exchanger will drive E_{Cl} and E_{HCO3} towards one another, namely depolarizing E_{Cl} and hyperpolarizing E_{HCO3} (Fig. 9E). This result may seem counterintuitive since the exchanger would be expected to play a helpful role in pH management. However, in the instance of another source of acidification, E_{HCO3} can undergo a hyperpolarizing shift, and the resultant change in HCO_3^- gradient can reverse Cl^-/HCO_3^- transport, driving Cl^- out and HCO_3^- in, thus preventing overt acidification (Fig. 9F).

These results predict that E_{Cl} can become more hyperpolarized during episodes of acidification. To test this, we modeled H^+ influx occurring over 5 seconds and monitored the time course of E_{Cl} during and after acidification in simulations with and without the Cl^-/HCO_3^- exchanger. In such simulations, proton influx triggers a reaction with HCO_3^- thus leading to a decrease in $[HCO_3^-]_i$. In turn, this leads to hyperpolarization of E_{HCO3} which will eventually become more hyperpolarized than E_{Cl}, effectively inverting the exchanger and leading to hyperpolarization of E_{Cl} (Fig. 9F). As the influx of H^+ is stopped, H^+ extrusion through the Na^+/H^+ exchange restores pH and the carbonic anhydrase mediated reaction is able to replenish intracellular HCO_3^-. As this slow change in $[HCO_3^-]_i$ translates into a change in the activity of the Cl^-/HCO_3^- exchanger, the value of E_{Cl} slowly becomes more depolarized until it returns to its resting value (Fig. 9F). As expected, these changes in E_{Cl} cannot be observed when simulations are conducted without the Cl^-/HCO_3^- exchanger (Fig. 9F). Thus, the Cl^-/HCO_3^- exchanger may be seen as a failsafe mechanism preventing overt acidification, at least when this acidification is not caused by HCO_3^- efflux through $GABA_A$ channels.

Accumulation of extracellular potassium influences $GABA_A$R-mediated current via a multi-step feedback loop

To extrude Cl^- from the cell, KCC2 must pass an equal number of K^+ ions since the net process is electroneutral. Therefore, K^+ efflux through KCC2 could reduce the transmembrane K^+ gradient and produce a depolarizing shift in E_K, which would, in turn, reduce Cl^- extrusion via KCC2 because of the reduction in KCC2 driving force. To investigate this putative negative feedback mechanism, we varied KCC2 activity and measured the impact on E_K (measured at the soma) in a model neuron receiving a fixed level of background excitatory and inhibitory synaptic input. Simulations showed that under conditions of distributed $GABA_A$R input at *in vivo*-like background frequencies, KCC2 activity actually had little impact on E_K unlike its large impact on E_{Cl} (Fig. 10A, compare *left* and *right* panels). We investigated this further by monitoring intra- and extracellular concentrations of K^+ (Fig. 10B). Although large in absolute terms, changes $[K^+]_i$ were small in relative terms, yielding much smaller shifts in E_K than those observed with E_{Cl}. Furthermore, KCC2 activity had only a small influence on $[K^+]_o$, which is controlled principally by the balance of K^+ leak conductance, active pumping by the Na^+-K^+-ATPase, and extracellular diffusion.

The insignificant effect of KCC2 activity on $[K^+]_o$ is apparently inconsistent with experimental observations [46], but those experiments involved applying a heavy Cl^- load, which is not comparable to the physiological conditions tested in Figure 10A and B. To test whether a larger Cl^- load could provoke a KCC2-mediated increase in $[K^+]_o$, we simulated a constant 5 nS, 500 ms-long $GABA_A$R conductance on a dendrite. Under those conditions, $[K^+]_o$ was significantly altered by KCC2 activity, as shown by the positive correlation between the maximal value of $[K^+]_o$ and KCC2 level (Fig. 10C). Repeating those simulations with reduced extracellular K^+ clearance confirmed that extracellular diffusion did not dramatically alter $[K^+]_o$ under these "heavy load" conditions (Fig. 10C). Regardless of whether KCC2 activity does or does not influence extracellular K^+ accumulation, extracellular K^+ accumulation is nonetheless expected to reduce the efficacy of KCC2 by reducing its driving force. To test this, we repeated the simulations shown in Figure 1D with different fixed values of $[K^+]_o$ and observed that the KCC2 efficacy is indeed reduced by the extracellular K^+ accumulation and stops passing ions when $[K^+]_o$ = 10 mM (Fig. 10D).

It is important to understand that changes in $[K^+]_o$ have a much larger effect on E_K than equivalent absolute changes in $[K^+]_i$. Hence, although KCC2 activity is not expected itself to change E_K under normal physiological conditions (see above), changes in E_K caused by other factors (*e.g.* high firing rates, reduced Na^+-K^+-ATPase activity, etc.) reduce KCC2 activity. In other words, there is no *closed* negative feedback loop directly linking KCC2 and E_K, but extrinsic factors can modulate Cl^- extrusion by affecting extracellular K^+ accumulation. Indeed, it is significant that Cl^- extrusion could be reduced (and inhibition thereby rendered ineffective) under conditions where excessive spiking (perhaps the result of disinhibition) causes extracellular K^+ accumulation – this would constitute a multi-step positive feedback loop (see also below).

Failure to control spiking increases chloride accumulation through a positive feedback loop that leads to catastrophic failure of inhibition

As shown in previous sections, $GABA_A$R input and KCC2 activity are prominent determinants of E_{Cl}. However, since Cl^- influx depends on the Cl^- driving force (*i.e.* $V - E_{Cl}$), variation in membrane potential will influence intracellular Cl^- accumulation, as shown in voltage clamp experiments [20]. Therefore, we predicted that increased depolarization caused by increased synaptic excitation would exacerbate intracellular Cl^- accumulation. To test this, the frequency of inhibitory synaptic events, f_{inh}, was fixed at 0.4 Hz/synapse while the frequency of excitatory synapses, f_{exc}, was varied (0.4 Hz was chosen for inhibitory events

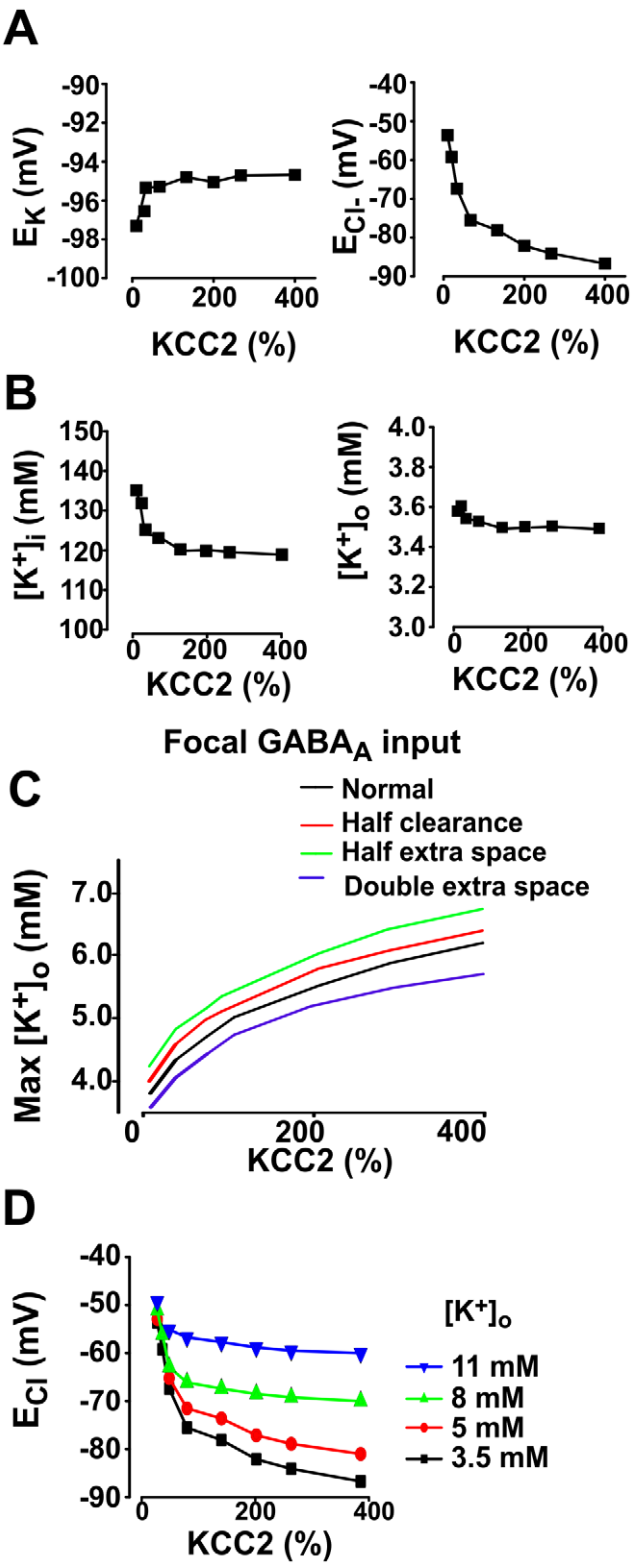

Figure 10. Interactions between $[Cl^-]$ regulation and $[K^+]$ regulation. A. Variation of KCC2 levels caused sizeable shifts in E_{Cl} (*right panel*) but had negligible effects on E_K (*left panel*). Background synaptic activity was f_{exc} = 0.2 Hz and f_{inh} = 0.8 Hz. **B.** Intra- and extracellular concentrations of K^+ for same simulations reported in **A**. Although extracellular K^+ levels are low, $[K^+]_o$ remains relatively stable due to other mechanisms, *e.g.* extracellular diffusion. This explains why E_K remains relatively constant in **A**. **C.** Maximal $[K^+]_o$ reached by applying a 500 nS GABA conductance to a dendrite. Time constant for diffusion from the FH space was tested at 100 and 200 ms (which corresponds to normal and 50% slower extracellular K^+ clearance) as well as with variable extracellular space. **D.** E_{Cl} as a function of the mean frequency of inhibitory input for various fixed levels of $[K^+]_o$.
doi:10.1371/journal.pcbi.1002149.g010

so that when f_{exc}/f_{inh} = 2, f_{exc} was still within its normal physiological range [24,30]). As predicted, the depolarizing shift in E_{Cl} scaled with f_{exc} (Fig. 11A). Moreover, given that spike generation makes membrane potential a highly nonlinear function of synaptic activity, we further predicted that the presence or absence of spiking would have a profound influence on $[Cl^-]_i$ because each spike represents a large, albeit short, increase in Cl^- driving force; in other words, if $GABA_AR$ channels are open during a spike, those spikes are expected to dramatically accelerate intracellular Cl^- accumulation. To test this, we measured Cl^- accumulation in a model with and without spikes (*i.e.* with and without HH channels, respectively). Results confirmed that Cl^- accumulation was indeed increased by spiking (Fig. 11B). The time series in Figure 11C shows the biphasic Cl^- accumulation associated with this phenomenon: When inhibition was first "turned on", it successfully prevented spiking but, over time, $[Cl^-]_i$ increased asymptotically toward some steady-state value. If the associated steady-state E_{GABA} was above spiking threshold (as in Fig. 11C), the membrane potential could increase beyond threshold and the neuron began spiking, at which point intracellular Cl^- began a second phase of accumulation. This second phase of Cl^- accumulation was paralleled by acceleration of the spike rate – clear evidence of the predicted positive feedback loop between spiking and Cl^- accumulation, which leads to catastrophic failure of inhibition.

To verify experimentally the model prediction that excitatory activity exacerbates intracellular Cl^- accumulation, especially when KCC2 activity is depleted, we performed $[Cl^-]_i$ measurements in primary cultured neurons exposed to muscimol, followed by addition of furosemide and kainate. The latter was to cause tonic activation of AMPA subtype glutamate receptors. As predicted by the model, addition of furosemide caused Cl^- accumulation in the cell, and subsequent application of kainate led to further accumulation (Fig. 11D).

The fact that E_{Cl} collapses as a result of $GABA_AR$ activity itself (Figs. 1, 3, 9) as well as excitatory input (Fig. 11A and D) and spiking (Fig. 11B and C) highlights the importance of treating E_{Cl} as a dynamic variable. To assess the importance of those dynamics on $GABA_AR$ modulation of the firing rate, we compared the relationship between firing rate and synaptic input in conditions where both inhibitory and excitatory input change in a proportional manner (*i.e.*, $f_{inh} \propto f_{exc}$). We performed simulations in which E_{Cl} was treated as a static value (as in conventional cable models) or as a dynamic variable (as in our electrodiffusion model). In the former case, E_{GABA} was fixed at -65 mV, while in the latter case, KCC2 activity was reduced to 33% of its normal level. With weak excitatory and inhibitory input, spiking was higher in the model with static E_{Cl} (Fig. 11E). However, as the frequencies of excitatory and inhibitory inputs were increased, all the mechanisms that contribute to a collapse of E_{Cl} (examined above) combined to drive f_{out} nonlinearly beyond the value predicted by fixed E_{Cl} (Fig. 11E). In short, these results show that E_{Cl} cannot be approximated by a single, static value when considering a range of stimulus conditions because of the rich dynamics governing E_{Cl} under natural conditions. Those dynamics can only be fully understood by accounting for numerous, interdependent biophysical processes.

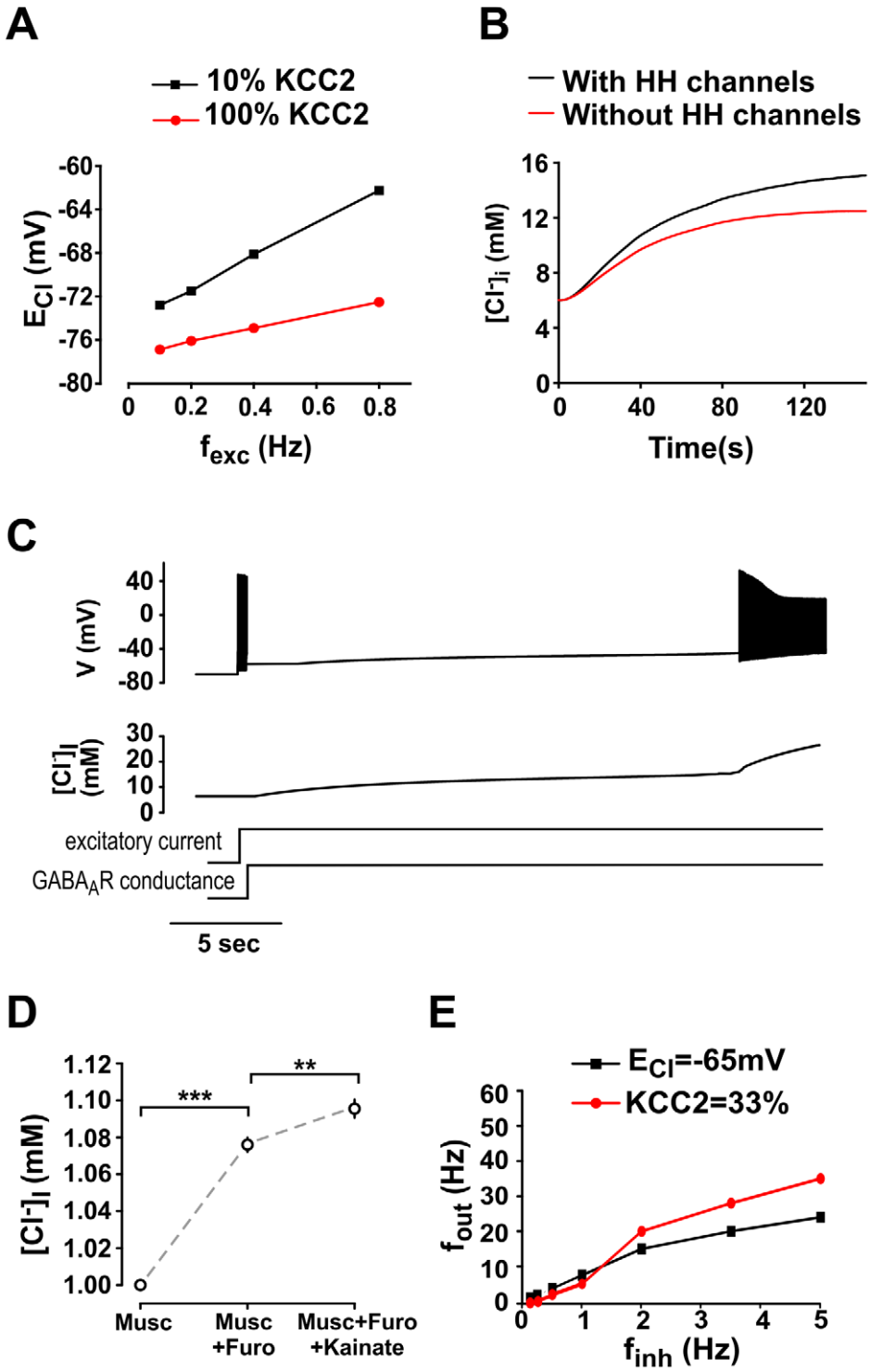

Figure 11. Effects of membrane potential on intracellular Cl^- accumulation. A. Varying the rate of excitatory synaptic drive (f_{exc}) caused a depolarizing shift in E_{Cl} secondary to changes in average membrane potential. f_{inh} was fixed at 0.4 Hz. **B.** Spiking exacerbates intracellular Cl^- accumulation as illustrated here by convergence of the model to different steady state $[Cl^-]_i$ depending on whether the model does or does not contain HH channels (*i.e.* does or does not spike, respectively). For this simulation, KCC2 activity was low (10%), f_{inh} = 0.8 Hz, and f_{exc} = 0.4 Hz. **C.** Sample traces showing inter-relationship between $[Cl^-]_i$ and spiking. Neuron began spiking when constant excitatory current was applied to the soma, but without any concomitant change in $[Cl^-]_i$ since there was not yet any $GABA_AR$-mediated conductance. Turning on constant $GABA_AR$ conductance in the soma terminated spiking, but at the expense of intracellular Cl^- accumulation. Chloride slowly accumulated over the next several seconds until membrane potential reached spike threshold, at which point spiking resumed and Cl^- began a second phase of accelerated accumulation. **D.** To test whether Cl^- accumulation is exacerbated by excitatory synaptic input in real neurons, somatic Cl^- concentration was measured using FLIM in neurons with or without glutamatergic receptor activation by kainate. As predicted by simulations, Cl^- accumulation was greater in neurons exposed to kainate. Furosemide was applied to block KCC2 activity in these experiments (**, $p < 0.001$; ***, $p < 0.0001$). Data from

56 cells from 5 coverslips. **E.** Comparison of input-output curve for static (*black*) vs. dynamic (*red*) E_{Cl}. Discrepancies between the curves clearly demonstrate that E_{Cl} cannot be approximated as constant value when considering a range of input conditions.
doi:10.1371/journal.pcbi.1002149.g011

Discussion

In this study, we built a neuron model that incorporates multiple processes controlling ion flux in order to investigate how interactions between those processes influence $GABA_AR$-mediated inhibition. This was prompted by the recognition that conventional neuron models make oversimplifying assumptions (*e.g.* reversal potentials are temporally invariant and spatially uniform or consider changes in only one ion specie) that are likely to be particularly consequential for $GABA_AR$-mediated inhibition. For instance, experiments have shown that E_{GABA} can shift during the course of sustained $GABA_AR$ input [2,42], that E_{GABA} is not uniform across different regions of the same neuron (our results and [26–28,46]) and that E_K has an important impact on Cl^- dynamics. Computational simulations are an ideal tool for investigating questions related to electrodiffusion and interaction between multiple ion species as well as for making predictions to guide subsequent experiments, but the accuracy of those simulations depends on the accuracy of the starting model. With that in mind, we built a neuron model that tracked $[Cl^-]$ changes as well as other ions that interact with $[Cl^-]$ homeostasis. Our model accurately reproduced activity-dependent decrease of IPSC amplitude, including differential decrease depending on the site of synaptic input and the compartment geometry [1,47]. Our model also reproduced spatial variations in E_{GABA} and its dependence on the interplay between strength of cotransporter activity and spatial distribution of $GABA_AR$ input. Having thus validated the model, we explored several other questions.

Upregulation of KCC2 has been linked with the hyperpolarizing shift in E_{GABA} observed during early development [7,20,45,48]. Likewise, downregulation of KCC2 has been linked with the depolarizing shift in E_{GABA} seen in various disease states [16,49,50]. However, the relationship between KCC2 and E_{GABA} has not heretofore been quantitatively explored. Simulations in our electrodiffusion model showed that that relationship is highly nonlinear: Reducing KCC2 activity caused a dramatic depolarizing shift in E_{GABA}, whereas increasing KCC2 activity above normal levels had only a small effect on E_{GABA}. The reason is that KCC2 already operates near its equilibrium point under normal conditions [51]. These observations suggest that therapies aiming to restore depleted KCC2 levels should not cause excessively strong $GABA_AR$-mediated inhibition if KCC2 overshoots its normal level. Moreover, the importance of investigating KCC2 regulation as a therapeutic target is emphasized by the observation that increasing the frequency or duration of $GABA_AR$ input cannot effectively compensate for disinhibition caused by KCC2 depletion since activity-dependent accumulation of intracellular Cl^- is increased under those conditions. In fact, our simulations illustrate how the optimal rate and time course of $GABA_AR$ input mutually influence each other and also depend on the level of KCC2 activity. Those observations help to explain why drugs that act by increasing $GABA_AR$ input have variable effects on the treatment of pathological conditions involving disrupted Cl^-homeostasis, e.g. in neuropathic pain or epilepsy. While administration of benzodiazepines has some efficacy at reversing tactile allodynia in neuropathic pain models, beyond a certain dose, they become counterproductive and enhance allodynia [52,53]. This bell shaped response to benzodiazepines on neuropathic pain follows directly the predictions from our model (Fig. 8).

Beyond helping understand pathological conditions, our model also provides insight into synaptic inhibition under normal conditions. The importance of interactions between Cl^- diffusion and transmembrane Cl^- flux became apparent when we considered the temporal dynamics of $[Cl^-]$. Simulations revealed that Cl^- accumulation near a highly active synapse is rapidly redistributed by intracellular diffusion, whereas Cl^- extrusion via KCC2 tends to act more slowly. The large volume of the soma keeps somatic $[Cl^-]_i$ relatively stable, in contrast to dendrites where diffusion is limited by the small diameter of the compartment. Thus, on short time scales, the soma acts as a Cl^- sink. It follows that the extent of Cl^- accumulation in dendrites does not only depend on the diameter of the dendrite, but also on the distance of the synapse from the soma. Since the dendrite diameter tends to decrease with the distance from the soma, the effects on diffusion are cumulative. As a result, diffusion is responsible for redistributing (and thus mitigating) transient, local changes in Cl^- load, while KCC2 level controls the steady-state balance of Cl^- influx and efflux. Thus, the faster dynamical collapse of E_{GABA} that occurs upon repetitive $GABA_AR$ input to distal dendrites results from limited diffusion rather than from inefficiency of Cl^- extrusion.

xThe functional impact of this result is that distributed synaptic input is more effective than clustered input, especially on distal dendrites where longitudinal Cl^- diffusion is particularly restricted. The more labile Cl^- gradient in distal dendrites causes a rapid collapse of $GABA_AR$-mediated hyperpolarization upon repetitive input, which limits its ability to influence somatic integration especially because, although remote current sources can hyperpolarize the soma, remote conductances do not cause shunting in the soma [1]. This implies that multiple GABAergic connections originating from the same presynaptic cell will be more effective if those synapses are distributed on different dendritic branches. It is interesting to note that this corresponds to the morphological arrangement observed in several systems [54]. This broad distribution contrasts the clustering of axo-axonic synapses that necessarily occurs when a presynaptic cell forms multiple synapses on a postsynaptic neuron's soma and AIS [54,55]. In the latter case, dynamical collapse of E_{GABA} does not occur because the soma acts as a Cl^- sink.

The functional impact of the standing $[Cl^-]_i$ gradient along the somato-dendritic axis resulting from the interplay between background $GABA_AR$ input and cotransporter activity may lead, under certain conditions, to differential impact of distal dendritic vs. somatic GABAergic synaptic input such as, for example, concurrent dendritic $GABA_A$-mediated excitation and somatic inhibition [1].

In addition to Cl^- dynamics, one must keep in mind that Cl^- flux does not occur independently from other ion species. For example, Cl^- influx through $GABA_AR$ is coupled with HCO_3^- efflux. The relationship between Cl^- flux and HCO_3^- flux is crucial for explaining how the net current through $GABA_AR$ can invert as Cl^- accumulates intracellularly [2,44]. Beyond causing a given shift in E_{GABA}, the HCO_3^- efflux has consequences on the dynamics of the system. Without HCO_3^- efflux, Cl^- influx would rapidly stabilize when membrane potential reached E_{GABA} because E_{GABA} would equal E_{Cl}. However, due to HCO_3^- efflux, and given that E_{GABA} is less negative than E_{Cl}, intracellular Cl^- continues to accumulate when the membrane potential initially reaches E_{GABA}. In the absence of other extrinsic factors and during sustained $GABA_AR$ input, intracellular Cl^- accumulation and membrane potential drift would progress until $E_{Cl} = E_{GABA} = E_{HCO3}$. This progression may, however, be prevented by the

influence of other intrinsic currents. In any case, HCO_3^- efflux effectively delays stabilization of the system until a more depolarized membrane potential is reached, which can make a crucial difference for whether or not membrane potential increases above spike threshold (see below). Consistent with these observations, a recent study showed that blocking carbonic anhydrase (and thereby presumably reducing HCO_3^- efflux through $GABA_AR$) can mitigate some of the behavioral manifestations of neuropathic pain thought to arise from KCC2 downregulation [52]. Moreover, based on their common reliance on HCO_3^-, regulation of $[Cl^-]_i$ competes with regulation of intracellular pH on long time scales (tens of seconds to minutes) consistent with experimental observations [3,24,56]. One functional consequence of this is that intracellular Cl^- accumulation (and, by extension, possibly the loss of KCC2 expression in pathological conditions) may act as a protective mechanism to prevent an excessive drop in intracellular pH during sustained $GABA_AR$ input.

The relationship between pH and Cl^- homeostasis may also be relevant to recent controversies regarding the necessity of ketone bodies for maintenance of E_{GABA} in the developing nervous system [57–60]. Given the HCO_3^- dependence of the beta-hydroxybutyrate effect on E_{GABA} in these experiments, it has been proposed that the explanation may reside in the fact that beta-hydroxybutyrate, lactate or pyruvate act as weak organic acids, thus acidifying the neuronal cytoplasm and reversing Cl^-/HCO_3^- exchange; this counteracts the drop in $[HCO_3^-]_i$ due to acidification but, by the same token, it lowers $[Cl^-]_i$ and drives E_{GABA} to a more negative value [59,61]. Our simulations are consistent with this explanation.

Given the coupled efflux of Cl^- and K^+ through KCC2, Cl^- extrusion happens at the expense of extracellular K^+ accumulation. This may appear counter-productive as extracellular K^+ accumulation counteracts inhibition and plays a role in the onset of epilepsy [62,63]. However, we found that under physiological conditions, K^+ efflux through KCC2 is offset by the fact that KCC2 activity enhances inhibition, thus decreasing firing rate and reducing K^+ efflux via transmembrane channels. The net effect is a reduction of excitability because K^+ efflux via transmembrane channels is larger than via KCC2. We found that this negative feedback stabilizes $[K^+]_o$ over a wide range of KCC2 activity. Disrupting this homeostasis requires sustained input from extrinsic factors. For example, intense GABAergic activity, which can maintain a continuous Cl^- load leading to a large and sustained K^+ efflux through KCC2, has been observed during giant depolarizing potentials [46]. Likewise, excessive spiking yields continuous extracellular K^+ accumulation, which renders KCC2 inefficient, causing a collapse of inhibition due to intracellular Cl^- accumulation.

Another interesting observation was that membrane depolarization tends to encourage intracellular Cl^- accumulation because Cl^- influx through $GABA_AR$ depends on Cl^- driving force, which is increased by depolarization. The consequences are profound: If sustained $GABA_AR$ input fails to prevent depolarization caused by concurrent excitatory input, the resulting depolarization will accelerate Cl^- influx, which in turn further reduces the $GABA_AR$-mediated outward current, thus supporting a positive-feedback cycle of failing inhibition. If the membrane potential reaches the spike threshold under these conditions, spike generation compounds the positive feedback process leading to an absolute failure of inhibition having potentially catastrophic consequences with respect to the neuron's response to stimulation. The only way for a neuron to avoid entering this vicious cycle is to regulate $[Cl^-]_i$, through Cl^- extrusion via KCC2.

In summary, we built a neuron model that incorporates multiple processes controlling the flux of different ion species in order to investigate how interactions between those processes influence inhibition mediated by $GABA_AR$. Many of those processes cooperate or compete with one another, thus producing nonlinearities. The most dramatic of those is arguably the catastrophic failure of inhibition that can develop when depolarization and spiking conspire with Cl^- accumulation to form a positive feedback loop. As demonstrated in this study, such details may be critical for understanding important aspects of synaptic inhibition, in particular, for understanding why and how inhibition fails under certain pathological conditions.

Methods

We built a conductance-based model of a whole neuron using the NEURON simulation environment [64] (model code will be made available at ModelDB). The model is composed of 30 dendritic compartments unless otherwise indicated, one somatic compartment, one compartment for the axon initial segment (AIS), and 10 myelinated axonal compartments separated by nodes of Ranvier. Details of the geometry are summarized in Figure 1A. Ionic currents flowing through channels, pumps and cotransporters were computed at each time step in order to update the membrane potential according to $C\frac{dV}{dt} = -\sum I$ where C is membrane capacitance of the neuron compartment and the sum is taken over synaptic currents, current through voltage gated channels and electrogenic Na-K ATPase. Transmembrane ion flux due to those currents was also calculated. Moreover, longitudinal and radial diffusion were incorporated into the model in order to account for intracellular ion gradients. Likewise, extracellular ionic diffusion was taken into account as well as chemical reactions that produce the various ion types (see below). Transmembrane ion flux, ion movement through diffusion, and ion generation through chemical reactions (Fig. 1B) were all taken into account when updating the concentration of ion specie x in each compartment at each time step according to the differential equation $\frac{d[x]_{i,o}}{dt} = \frac{\pm I_x}{(z \cdot F \cdot Vol)} + \frac{Diff_x}{Vol} + \frac{Reac_x}{Vol}$, where F is the Faraday constant, z is the ion valence, Vol is the compartment volume, $Reac_x$ is a term accounting for chemical reactions involving ion species x and $Diff_x$ is a term modeling the *electrodiffusion* of ion x [65,66]. Synaptic events are expressed in currents, but the membrane potential was not clamped, consistent with realistic conditions. This is of importance since invasive cell manipulations have been shown to alter the nature (inhibitory or excitatory) of $GABA_A$ mediated input [67].

Channels

Ion currents obey the equation $I_x = g_x(V - E_x)$ where E_x denotes the reversal potential for ion x and g_x is the channel conductance with respect to ion x. Reversal potentials were continuously updated during the simulation using the Nernst equation $E_x = z\left(\frac{R \cdot T}{F}\right)\log\left(\frac{[x]_o}{[x]_i}\right)$ where R is the perfect gas constant and T is absolute temperature, which was taken to be 310°K (37°C). Because $GABA_A$ receptors pass both Cl^- and HCO_3^- anions in a 4:1 ratio [24], E_{GABA} was calculated using the Goldman-Hodgkin-Katz equation

$$E_{GABA} = -\left(\frac{RT}{F}\right)\log\left(\frac{4[Cl^-]_o + [HCO_3^-]_o}{4[Cl^-]_i + [HCO_3^-]_i}\right).$$

Each of these ionic currents was taken into account for computing change in concentration of their respective ion species

and their sum yielded the net current used to update the membrane potential.

Synaptic input was modeled as a Poisson process. Each inhibitory synapse was activated at a mean frequency of 0–10 Hz and each excitatory synapse was activated at a mean frequency of 0–2 Hz. Unless otherwise stated, the maximal conductance of inhibitory synapses was 1±0.3 nS (mean ± standard deviation) and kinetics were modeled as instantaneous rise and exponential decay with τ_{IPSC} of 30 ms [30,68–70]. $GABA_AR$ synaptic density was 60 synapses per 100 μm^2 in the AIS, 40 synapses per 100 μm^2 in the soma and 12 synapses per 100 μm^2 in the dendrites. Density of excitatory synapses was 60 synapses per 100 μm^2 in dendrites and no excitatory synapses were present elsewhere [21,30]. Unless otherwise stated, the maximal conductance of excitatory synapses was taken to be 0.5±0.2 nS (mean ± standard deviation) and the kinetics were modeled as an instantaneous rise and exponential decay with τ_{EPSC} of 10 ms.

Hodgkin-Huxley (HH) channels were modeled using parameter values reported by [12]. The voltage-dependant Na^+ current was given by

$$I_{Na} = \bar{g}_{Na} m^3 h (V - E_{Na})$$
$$\frac{dm}{dt} = \alpha_m(V)(1-m) - \beta_m(V)m$$
$$\frac{dh}{dt} = \alpha_h(V)(1-h) - \beta_m(V)h$$
$$\alpha_m = \frac{-0.32(V - V_T - 13)}{\exp[(V - V_T - 40)/5] - 1}$$
$$\beta_m = \frac{0.28(V - V_T - 40)}{\exp[(V - V_T - 40)/5] - 1}$$
$$\alpha_h = 0.128 \exp[-(V - V_T - V_s - 17)/18]$$
$$\beta_h = \frac{4}{1 + \exp[-(V - V_T - V_s - 40)/5]}$$

Where $V_T = -58$ mV and $V_S = -10$ mV. The voltage gated K^+ channels were described by

$$I_K = g_K n^4 (V - E_K)$$
$$\frac{dn}{dt} = \alpha_n(V)(1-n) - \beta_n(V)n$$
$$\alpha_n = \frac{-0.032(V - V_T - 15)}{\exp[-(V - V_T - 15)/5] - 1}$$
$$\beta_n = 0.5 \exp[-(V - V_T - 10)/40]$$

The density of HH channels was 12 mS/cm^2 in the AIS and 1.2 mS/cm^2 in soma and dendrites [21,30]. The model also included K^+ and Na^+ leak channels with respective densities of 0.02 mS/cm^2 and 0.004 mS/cm^2 in soma, 0.03 mS/cm^2 and 0.006 mS/cm^2 in proximal dendrites, 0.1 mS/cm^2 and 0.02 mS/cm^2 in distal dendrites, 0.02 μS/cm^2 and 0.004 μS/cm^2 in axon internodes, and 15 mS/cm^2 and 3 mS/cm^2 in axon nodes as described in [21,30].

For some simulations, we added other types of conductances to account for the many possible types of spike generating mechanisms. Namely, we added non-inactivating Ca^{2+}-activated K^+ channels and persistent Na^+ channels to test spike reducing and spike enhancing mechanisms, respectively. The Ca^{2+}-activated K^+ channels obey the following sets of equations

$$I_{K,Ca} = g_{K,Ca} m^3 z^2 h (V - E_K)$$
$$\frac{dm}{dt} = \frac{m_\infty - m}{\tau_m},$$
$$\frac{dz}{dt} = \frac{z_\infty - z}{\tau_z},$$
$$\frac{dh}{dt} = \frac{h_\infty - h}{\tau_h}.$$

Where the auxiliary functions are defined by

$$m_\infty = \frac{1}{1 + \exp(-(V - c_{vm})/c_{km})}$$
$$\tau_m = \frac{1}{\exp(-(V + c_{vtm1})/c_{ktm1}) + \exp(-(V - c_{vtm2})/c_{ktm2})},$$
$$z_\infty = \frac{1}{1 + z_{half}/[Ca^{2+}]_i},$$
$$h_\infty = ch + \frac{1 - ch}{1 + \exp(-(V + c_{vh})/c_{kh})},$$
$$\tau_h = \frac{1}{\exp(-(V + c_{vth1})/c_{kth1}) + \exp(-(V - c_{vth2})/c_{kth2})}.$$

With the constants defined as c_{vm} = 28.9 mV, c_{km} = 6.2 mV, ctm = 0.000505 s, c_{vtm1} = 86.4 mV, c_{ktm1} = -10.1 mV, c_{vtm2} = -33.3 mV, c_{ktm2} = 10 mV. τ_z = 1 s, ch = 0.085, c_{vh} = 32 mV, c_{kh} = -5.8 mV, c_{th} = 0.0019 s, c_{vth1} = 48.5 mV, c_{kth1} = -54.2 mV, c_{vth2} = -54.2 mV, c_{kth2} = 12.9 mV.

The persistent Na^+ channels were described by the following set of equations:

$$I_{Na,P} = g_{Na,P} m h (V - E_{Na}),$$
$$\frac{dm}{dt} = \frac{m_\infty - m}{\tau_m},$$
$$\frac{dh}{dt} = \frac{h_\infty - h}{\tau_h}.$$

Where the auxiliary functions are defined by

$$\tau_m = \left(\frac{0.32(v_{sm} + 13 - V)}{\exp\left(\frac{v_{sm} + 13 - V}{4}\right) - 1} + \frac{0.28(v_{sm} + V - 40)}{\exp\left(\frac{v_{sm} + V - 40}{5}\right) - 1} \right)^{-1}$$
$$m_\infty = \frac{0.32(v_{sm} + 13 - V)}{\exp\left(\frac{v_{sm} + 13 - V}{4}\right) - 1}$$
$$\left(\frac{0.32(v_{sm} + 13 - V)}{\exp\left(\frac{v_{sm} + 13 - V}{4}\right) - 1} + \frac{0.28(v_{sm} + V - 40)}{\exp\left(\frac{v_{sm} + V - 40}{5}\right) - 1} \right)^{-1}$$
$$\tau_h = \frac{1}{0.128 \exp((v_{sh} + 17 - V)/18) + \frac{4}{1 + \exp((v_{sh} + 40 - V)/2.5)}}$$
$$h_\infty = \frac{0.128 \exp((v_{sh} + 17 - V)/18)}{0.128 \exp((v_{sh} + 17 - V)/18) + \frac{4}{1 + \exp((v_{sh} + 40 - V)/2.5)}}$$

Where the constants are given by $v_{sm} = -2$ mV and $v_{sh} = -5$ mV.

Finally, to account for non-synaptic, tonically activated Cl^- conductance, in some simulations we added $GABA_A$ leak channels with the same ratio of Cl^-:HCO_3^- permittivity as the synaptic channels, the density of such channels was 0.003 mS/cm^2 in soma, 0.0045 mS/cm^2 in proximal dendrites, 0.015 mS/cm^2, 0.003 μS/cm2 in axon internodes and 2.3 mS/cm^2 in axon nodes.

Sodium-potassium pump and cation-chloride cotransporters

The Na^+-K^+-ATPase pump uses the energy from hydrolysis of one ATP molecule to pump three Na^+ ions out of the neuron and two K^+ ions inside. The activity of this pump is dependent on $[K^+]_o$ and $[Na^+]_i$ as well as on the membrane potential as observed in [71]. The Na^+ current through the pump is given by the following equations

$$I_{Na,K} = \overline{I_{Na,K}} \frac{f_{Na,K}}{\left(1 + \frac{K_{m,Nai}}{[Na^+]_i}\right)^{1.5}} \frac{[K^+]_o}{[K^+]_o + K_{m,Ko}}$$

$$f_{Na,K} = \frac{1}{1 + 0.1245 \exp\left(\frac{-0.0001 V_m F}{RT}\right)} + 0.365\sigma \exp\left(\frac{-0.001 V_m F}{RT}\right)$$

$$\sigma = \frac{\exp\left(\frac{[Na^+]_o}{Na_{Half}}\right) - 1}{7}$$

[72,73]. With $K_{m,Ko} = 1.5$ mM, $K_{m,Nai} = 10$ mM and $Na_{Half} = 20$ mM. The outgoing Cl^- flux though KCC2 was modeled according to [2,4] by

$$I_{Cl,KCC2} = \frac{I_{Cl,\max}(E_K - E_{Cl})}{(E_K - E_{Cl}) + V_{half}}.$$

The K^+ current through KCC2 was assumed to be equal in absolute value but opposite in polarity to the Cl^- current so that net current through KCC2 was equal to zero. The maximal Cl^- current going through KCC2 was taken to be $I_{Cl,max} = 0.3$ mA/cm^2 for the normal activity level. This value was chosen to give $E_{Cl} = -80$ mV when mean synaptic input frequencies were 3.2 Hz and 1.6 Hz for inhibition and excitation, respectively. This value also turned out to yield maximal Cl^- clearance rates near 10 mM/s, consistent with experimental data [4]. The value of the driving force (E_{Cl}-E_K) at which the Cl^- current through KCC2 reaches its half maximal value (V_{half}) was set to 40 mV. This corresponds to $[Cl^-]_i = 15$ mM under the assumption that $[Cl^-]_o = 120$ mM and $E_K = -95$ mV.

In some simulations, we also modeled NKCC1 activity in the AIS. The Cl^- influx through NKCC1 was modeled by

$$I_{Cl,NKCC1} = \frac{I_{Cl,\max}(E_{NKCC1} - E_{Cl})}{(E_{NKCC1} - E_{Cl}) + V_{half}}.$$

Where E_{NKCC1} is the value of E_{Cl} at which Cl^- flow through NKCC1 reverses direction and is given by $E_{NKCC1} = (E_K + E_{Na})/2$. The maximal Cl^- current going through NKCC1 was taken to be $I_{Cl,max} = 0.3$ mA/cm^2 for the normal activity level which was taken to equal the value obtained for maximal current through KCC2. Na^+ and K^+ currents through NKCC1 were each half of $I_{Cl,NKCC1}$ so that net current through NKCC1 was equal to zero.

Finally, in some simulations we also modeled the Cl^-/HCO_3^- exchanger which was assumed to be ubiquitous in the neuron and uniformly distributed on the membrane. Kinetics of the exchanger were described by the following simplified equation.

$$I_{Cl,exch} = \frac{I_{Cl,\max}(E_{HCO3} - E_{Cl})}{(E_{HCO3} - E_{Cl}) + V_{half}}$$

where *ICl,max* = 0.1 mA/cm^2 and *Vhalf* was set to 50 mV. The $HCO3^-$ and Cl^- currents through the exchanger were taken to be equal in amplitude but opposite in direction so that the exchange process is electroneutral.

Bicarbonate and pH management

Since HCO_3^- ions also flow through $GABA_AR$ channels (see above), it was important to model the ionic fluxes and reactions regulating $[HCO_3^-]$. Intracellular HCO_3^- loss due to outgoing flux via $GABA_AR$ is compensated by the carbonic anhydrase-catalyzed reaction $CO_2 + H_2O \leftrightarrow H^+ + HCO_3^-$ [3,44,56,74]. Since the diffusion of CO_2 gas through the membrane is faster than ionic fluxes through channels, we treated pCO_2 as constant. The equilibrium constant of the reaction was $10^{-6.35}$ M and the rate constant for CO_2 hydration was 10^6 sec^{-1} [75]. Since the above reaction produces a drop in pH [42,44,56] by causing intracellular H^+ accumulation, we also modeled the reaction between H^+ and the main buffering ion $H_2PO_4^-$ such that H^+ buffering occurred through the reaction $H^+ + HPO_4^{2-} \leftrightarrow H_2PO_4^-$. Although other reactions play important roles in pH buffering, we kept the model as simple as possible while preserving the global value of pH buffering capacity, estimated to be 25–30 mMol/pHU [76,77]. Buffering reactions are responsible for maintaining the pH value constant at short time scales (~100 ms), but proton extrusion via exchangers plays an important role on longer time scales (>10s). For the sake of simplicity, we limited ourselves to modeling the Na^+-H^+ exchanger such that the proton flux was given by

$$I_{H,NaH} = I_{H,\max} \frac{(E_{Na} - E_H)}{(E_{Na} - E_H) + V_{half}}$$

which is a generic scheme for transporters. We used $I_{H,max} = 0.03$ mA/cm^2 and $V_{half} = 10$ mV. These values were chosen to make the model consistent with the global proton extrusion rate in healthy neurons that has been measured to be 0.04 pHU/s [78–80].

Electrodiffusion

An important and novel feature of the model is that the intra- and extracellular concentrations of K^+, Na^+, Ca^{2+}, Cl^-, HCO_3^- as well as intracellular concentrations of H^+, HPO_4^{2-} and $H_2PO_4^-$ were treated as dynamical variables updated in each compartment at each time step. Each compartment was divided in four concentric annulus-shaped subcompartments to account for radial diffusion. Diffusion coefficients were assumed to be the same as in water (in 10^{-5} cm^2/s): 2.03 for Cl^-, 1.33 for Na^+, 1.96 for K^+, and 9.33 for H^+ [81]. Longitudinal *electrodiffusion* is described by the equation $\frac{Vol\partial[x]_i}{\partial t} = D_x Surf \frac{\partial^2[x]_i}{\partial y^2} + \frac{D_x Surf}{z}\frac{\partial}{\partial y}\left([x]_i \frac{\partial V}{\partial y}\right)$ where y stands for the longitudinal axis, D_x for the diffusion coefficient with respect to ion specie x, *Vol* for section volume and *Surf* for the surface of the cross section [66].

The first term is due to pure diffusion while the second term accounts for the electrical force acting on the ions. The second term was used only to compute electrodiffusion between outer annuli of dendritic sections and was set to 0 for inner annuli, consistent with the fact that electrical field extends only to a thin region near the membrane. This is because the membrane act as a capacitor and electric field is known to decrease rapidly [82]. Radial diffusion was computed in a similar way but with y representing the radial axis.

Extracellular space was represented as a thin shell (i.e. Frankenhaeuser-Hodgkin or FH space) with equivalent volume equal to one fourth the intracellular volume of the corresponding cell compartment. The inner surface of the FH space communicated with the adjacent intracellular compartment while the outer surface was linked to an infinite reservoir where ion concentrations were assumed to be constant. This modeling takes into account changes in $[K^+]_o$ due only to our cell, and thus does not address changes in $[K^+]_o$ due to network activity. The study of such network related effects is beyond the scope of the current study. The equation used to update extracellular ion concentration is given by $\frac{d[x]_o}{dt} = \frac{-I_x}{(z \cdot F \cdot Vol)} + \frac{Diff_x}{Vol} + \frac{([x]_o - k_{bath})}{\tau_{FH}}$ where z is the ion valence, k_{bath} is the concentration of ion x in the infinite reservoir and τ_{FH} is the time constant taken to be 100 ms [79,83].

Numerical methods

The differential equations were integrated using a forward Euler method with a time step of 0.05 ms. Several preliminary simulations showed this time step to be both sufficiently small for accurate equation solving, while sufficiently large for reasonably fast computing. Initial intracellular concentrations were (in mM): $[Cl^-]_i = 6$, $[K^+]_i = 140$, $[Na^+]_i = 10$, $[HCO_3^-]_i = 15$ $[H_2PO_4^-]_i = 30$ and $[HPO_4^{2-}]_i = 30$. Initial extracellular concentrations were in (mM) $[Cl^-]_o = 120$, $[K^+]_o = 3$, $[Na^+]_o = 45$ and $[HCO_3^-]_o = 25$ [81]. Preliminary simulations were conducted to determine initial concentrations such that they were stable under normal conditions (in the absence of high frequency synaptic input). For simulations in which the value of maximal Cl^- current through KCC2 ($I_{Cl,KCC2}$) was different than the normal one stated above ($I_{Cl,max} = 0.3$ mA/cm^2), different initial values of $[Cl^-]_i$ were used in order to start the simulation near steady state, as determined by preliminary testing. Unless stated otherwise, simulations were run for 200 s of simulated time, short enough to allow manageable simulations and long enough to allow collection of sufficiently large data sample to insure relevance of mean values.

Cell cultures

Dissociated hippocampal neurons from Sprague-Dawley rats were prepared as previously described [84] plated at P0 to P2 at a density of approximately 500–600 cells/mm^2 and imaged after 21–30 days in vitro (DIV). Glial proliferation was stopped at 5 DIV with Ara-C.

Chloride imaging

Cells were loaded in a 5 mM solution of the Cl^- indicator MQAE (*N*-6-methoxyquinolinium acetoethylester; Molecular Probes) for 30 min at 37 °C [85]. Prior to observation, cells were transferred to a perfusion chamber and bathed in bicarbonate-buffered saline containing: 100 NaCl, 2.5 KCl, 1 NaH_2PO_4, 26 $NaHCO_3$, 1 $MgCl_2$ and 1.2 $CaCl_2$. Muscimol (100 µM, Tocris), furosemide (50-200 µM, Sigma), kainic acid (50 nM, Tocris), VU 0240551 (25-50 µM, Tocris) and bicuculine (100 µM, Sigma) were selectively added as described in the result section. Upon addition of drugs, cells were allowed to adjust for 10–20 minutes before a steady-state image of their Cl^- contents was taken.

Fluorescence lifetime images of MQAE were acquired using a Becker & Hickl SPC-830 module coupled to a Zeiss LSM 510 microscope. MQAE was excited using a femtosecond pulsed Ti-Sapphire laser tuned at 760 nm (Chameleon Ultra, Coherent), through a 40X water-immersion objective (Zeiss, 0.8 NA). Fluorescence lifetime data was collected through the non-descanned port of the microscope using a band-pass filter (469/35 nm, Semrock) coupled to a laser block (short-pass 750 nm; Semrock). Photon emission was detected using a PMC-100-1 photosensor (Hamamatsu). Lifetime in each cell compartment was calculated and extracted using SPCImage software (Becker & Hickl). Lifetime in the cell body was averaged over the total cell body area excluding the nucleus region, whereas in the dendrites it was averaged in segments of 4 µm over 120 µm of dendrite length. Fluorescence lifetime measurements were used because they are not sensitive to dye concentration (peak intensity) in the range we are using [85,86]. The lifetime measurements are thus not affected by differences in dye loading from cell to cell or by volume changes that could occur in different cell compartments (Fig. 2A). The Cl^- dependence of MQAE lifetime is described by the Stern-Volmer relation ($\tau_0/\tau = 1 + Ksv\,[Cl^-]_i$), where τ_0 is the fluorescence lifetime in 0 mM Cl^-, and Ksv, the Stern-Volmer constant, is a measure of the Cl^- sensitivity of MQAE (Fig. 2B).

Chloride calibration in cells

For calibration of absolute Cl^- concentrations, the fluorescence lifetime of MQAE-loaded cells was measured in the presence of different known extracellular $[Cl^-]$ (8, 15 or 20 mM) in the bath. To dissipate the Cl^- gradient across the membranes, 20 µM tributyltin (Cl^--OH exchanger) was used and 20 µM nigericin (K^+-H^+ exchanger) was added to clamp the intracellular pH using high K^+ driving force while Cl^- changes. Calibration solutions contained (in mM) KCl and KNO_3 (140 K^+ total with desired amount Cl^-), 10 D-glucose, 10 HEPES, 1.2 $CaCl_2$, 1 $MgCl_2$, pH adjusted to 7.2 using KOH.

Immunocytochemistry

Primary hippocampal cultures (5 and 28 DIV) were fixed for 10 min with 4% paraformaldehyde and then permeabilized for 45 min with 0.2% triton in 10% normal goat serum (NGS). Primary antibody incubations were performed overnight at 4 °C using a polyclonal marker of KCC2 (Rabbit anti-KCC2 1:500, Upstate) in the presence of 5% NGS. Alexa 546 conjugated secondary antibodies (1:750; Invitrogen, Eugene, OR) were applied for 2 hrs at room temperature. Images were obtained on the Zeiss LSM 510 microscope using a 63X/1.4NA oil objective (Zeiss).

Spatial intensity distribution analysis (SpIDA)

SpIDA is a recently developed analysis method that can resolve concentration of mixtures of different monomeric and oligomeric labels in single fluorescence images by fitting its intensity histogram. Precise details of the technique and detector calibration are presented in [33]. Briefly, the intensity histogram fitting function for a system with density *of N* particles is:

$$H(\varepsilon,N;k) = \sum_n \rho^n(\varepsilon;k) \cdot poi(n,N) \text{with} \rho^0(\varepsilon;k) = \delta_{k,0}$$

Where $\rho^n(\varepsilon;k) = \rho^1(\varepsilon;k) \otimes \rho^{n-1}(\varepsilon;k)$ with $\rho^1(\varepsilon;k) = \int \delta(\varepsilon \cdot I(\mathbf{r}) - k) d\mathbf{r}\, I(\mathbf{r})$ is the illumination intensity profile of the excitation laser, ε represents the quantal brightness of a single fluorescent

particle, and k is the probability of observing an *intensity* of light (assumed to be proportional the number of photons emitted). H is normalized over all intensity values so the integral over k gives one. A constant factor, A, is introduced, which is the number of pixels in an analyzed region of the image where the fluorescent particles are distributed. This allows for the fit of an image intensity histogram to be performed. Three parameters are fit: the number of pixels (A), the fluorescent particle density (N particles per laser beam effective focal volume) and the quantal brightness (ε intensity units, iu, per unit of pixel integration time). In confocal laser scanning microscopes, the fluorescence intensity is measured using photon multiplier tubes (PMTs), and the number of collected photoelectrons is a function of the polarization voltage.

If dimers are present in the sample, they will yield quantal brightness of 2ε. When the monomer and dimer populations are mixed within the same region in space, the total histogram becomes the convolution of the two individual distributions:

$$H(\varepsilon_1,N_1,\varepsilon_2,N_2,A;k) = A\cdot H(\varepsilon 1,N_1;k)\otimes H(\varepsilon_2,N_2;k)$$

To obtain accurate results, noise characteristics of the detector also has to be studied and taken into account in the analysis, See [33] for complete analysis.

For each sample, an optimal setting of the laser power and PMT voltage was chosen to minimize pixel saturation and photobleaching. The CLSM settings were kept constant for all samples and controls (Laser power, filters, dichroic mirrors, polarization voltage, scan speed). Acquisition parameters were always set within the linear range of the detector which was determined by calibration [33]. All the images were 1024×1024 pixels with pixel size of 0.115 μm and 9.1 μs pixel dwell time. The z-stacks were taken by optical sectioning with a z step of 0.5 μm per image.

Ethics statement

All experiments were performed in accordance with regulations of the Canadian Council on Animal Care.

Author Contributions

Conceived and designed the experiments: ND SAP AC AGG YDK. Performed the experiments: AC. Analyzed the data: ND AC AGG. Contributed reagents/materials/analysis tools: ND AGG. Wrote the paper: ND SAP AC AGG HK YDK.

References

1. Hausser M, Major G, Stuart GJ (2001) Differential shunting of EPSPs by action potentials. Science 291: 138–141.
2. Staley KJ, Soldo BL, Proctor WR (1995) Ionic mechanisms of neuronal excitation by inhibitory GABAA receptors. Science 269: 977–981.
3. Kaila K, Voipio J (1987) Postsynaptic Fall in intracellular pH induced by GABA-activated bicarbonate Cconductance. Nature 330: 163–165.
4. Staley KJ, Proctor WR (1999) Modulation of mammalian dendritic $GABA_A$ receptor function by the kinetics of Cl^- and HCO_3^- transport. J Physiol 519: 693–712.
5. Prescott SA, Sejnowski TJ, De Koninck Y (2006) Reduction of anion reversal potential subverts the inhibitory control of firing rate in spinal lamina I neurons: towards a biophysical basis for neuropathic pain. Mol Pain 2: 32.
6. Blaesse P, Airaksinen MS, Rivera C, Kaila K (2009) Cation-Chloride Cotransporters and Neuronal Function. Neuron 61: 820–838.
7. Rivera C, Voipio J, Payne JA, Ruusuvuori E, Lahtinen H, et al. (1999) The K^+/Cl^- co-transporter KCC2 renders GABA hyperpolarizing during neuronal maturation. Nature 397: 251–255.
8. Brumback AC, Staley KJ (2008) Thermodynamic regulation of NKCC1-mediated Cl^- cotransport underlies plasticity of $GABA_A$ signaling in neonatal neurons. J Neurosci 28: 1301–1312.
9. Coull JA, Boudreau D, Bachand K, Prescott SA, Nault F, et al. (2003) Trans-synaptic shift in anion gradient in spinal lamina I neurons as a mechanism of neuropathic pain. Nature 424: 938–942.
10. Coull JA, Beggs S, Boudreau D, Boivin D, Tsuda M, et al. (2005) BDNF from microglia causes the shift in neuronal anion gradient underlying neuropathic pain. Nature 438: 1017–1021.
11. Dzhala VI, Staley KJ (2003) Excitatory actions of endogenously released GABA contribute to initiation of ictal epileptiform activity in the developing hippocampus. J Neurosci 23: 1840–1846.
12. Glykys J, Staley KJ (2008) Differences in cortical vs. subcortical GABA effects: A mechanism for electroclinical dissociation of neonatal seizures. Epilepsia 49: 170.
13. Huberfeld G, Wittner L, Clemenceau S, Baulac M, Kaila K, et al. (2007) Perturbed chloride homeostasis and GABAergic signaling in human temporal lobe epilepsy. J Neurosci 27: 9866–9873.
14. Kahle KT, Staley KJ (2008) The bumetanide-sensitive Na-K-2Cl cotransporter NKCC1 as a potential target of a novel mechanism-based treatment strategy for neonatal seizures. Neurosurg Focus 25: E22.
15. Payne JA, Rivera C, Voipio J, Kaila K (2003) Cation-chloride co-transporters in neuronal communication, development and trauma. Trends Neurosci 26: 199–206.
16. De Koninck Y (2007) Altered chloride homeostasis in neurological disorders: a new target. Curr Opin Pharmacol 7: 93–99.
17. Woodin MA, Ganguly K, Poo MM (2003) Coincident pre- and postsynaptic activity modifies GABAergic synapses by postsynaptic changes in Cl^- transporter activity. Neuron 39: 807–820.
18. Chabwine JN, Van Damme P, Eggermont J, De Smedt H, Missiaen L, et al. (2004) Long-lasting changes in GABA responsiveness in cultured neurons. Neurosci Lett 365: 69–72.
19. Jedlicka P, Deller T, Gutkin BS, Backus KH (2010) Activity-dependent intracellular chloride accumulation and diffusion controls $GABA_A$ receptor-mediated synaptic transmission. Hippocampus 29: 509–519.
20. Cordero-Erausquin M, Coull JA, Boudreau D, Rolland M, De Koninck Y (2005) Differential maturation of GABA action and anion reversal potential in spinal lamina I neurons: impact of chloride extrusion capacity. J Neurosci 25: 9613–9623.
21. Destexhe A, Rudolph M, Pare D (2003) The high-conductance state of neocortical neurons in vivo. Nat Rev Neurosci 4: 739–751.
22. Rivera C, Voipio J, Thomas-Crusells J, Li H, Emri Z, et al. (2004) Mechanism of activity-dependent downregulation of the neuron-specific K-Cl cotransporter KCC2. J Neurosci 24: 4683–4691.
23. Rivera C, Li H, Thomas-Crusells J, Lahtinen H, Viitanen T, et al. (2002) BDNF-induced TrkB activation down-regulates the K^+-Cl^- cotransporter KCC2 and impairs neuronal Cl^- extrusion. J Cell Biol 159: 747–752.
24. Voipio J, Pasternack M, Rydqvist B, Kaila K (1991) Effect of Gamma-Aminobutyric-Acid on Intracellular pH in the Crayfish Stretch-Receptor Neuron. J Exp Biol 156: 349–361.
25. Delpire E, Days E, Lewis LM, Mi D, Kim K, et al. (2009) Small-molecule screen identifies inhibitors of the neuronal K-Cl cotransporter KCC2. Proc Natl Acad Sci U S A 106: 5383–5388.
26. Berglund K, Schleich W, Krieger P, Loo LS, Wang DQ, et al. (2006) Imaging synaptic inhibition in transgenic mice expressing the chloride indicator, Clomeleon. Brain Cell Biol 35: 207–228.
27. Berglund K, Schleich W, Wang H, Feng GP, Hall WC, et al. (2008) Imaging synaptic inhibition throughout the brain via genetically targeted Clomeleon. Brain Cell Biol 36: 101–118.
28. Khirug S, Yamada J, Afzalov R, Voipio J, Khiroug L, et al. (2008) GABAergic depolarization of the axon initial segment in cortical principal neurons is caused by the Na-K-2Cl cotransporter NKCC1. J Neurosci 28: 4635–4639.
29. Duebel J, Haverkamp S, Schleich W, Feng GP, Augustine GJ, et al. (2006) Two-photon imaging reveals somatodendritic chloride gradient in retinal ON-type bipolar cells expressing the biosensor clomeleon. Neuron 49: 81–94.
30. Destexhe A, Pare D (1999) Impact of network activity on the integrative properties of neocortical pyramidal neurons in vivo. J Neurophysiol 81: 1531–1547.
31. Blaesse P, Guillemin I, Schindler J, Schweizer M, Delpire E, et al. (2006) Oligomerization of KCC2 correlates with development of inhibitory neurotransmission. J Neurosci 26: 10407–10419.
32. Uvarov P, Ludwig A, Markkanen M, Soni S, Hubner CA, et al. (2009) Coexpression and heteromerization of two neuronal K-Cl cotransporter isoforms in neonatal brain. J Biol Chem 284: 13696–13704.
33. Godin AG, Costantino S, Lorenzo LE, Swift JL, Sergeev M, et al. (2011) Revealing protein oligomerization and densities in situ using spatial intensity distribution analysis. Proc Natl Acad Sci U S A 108: 7010–7015.
34. Swift JL, Godin AG, Dore K, Freland L, Bouchard N, et al. (2011) Quantification of receptor tyrosine kinase transactivation through direct dimerization and surface density measurements in single cells. Proc Natl Acad Sci U S A 108: 7016–7021.
35. Costantino S, Kent CB, Godin AG, Kennedy TE, Wiseman PW, et al. (2008) Semi-automated quantification of filopodial dynamics. J Neurosci Methods 171: 165–173.
36. Gulyas AI, Sik A, Payne JA, Kaila K, Freund TF (2001) The KCl cotransporter, KCC2, is highly expressed in the vicinity of excitatory synapses in the rat hippocampus. Eur J Neurosci 13: 2205–2217.

37. Li H, Khirug S, Cai C, Ludwig A, Blaesse P, et al. (2007) KCC2 interacts with the dendritic cytoskeleton to promote spine development. Neuron 56: 1019–1033.
38. Gulacsi A, Lee CR, Sik A, Viitanen T, Kaila K, et al. (2003) Cell type-specific differences in chloride-regulatory mechanisms and $GABA_A$ receptor-mediated inhibition in rat substantia nigra. J Neurosci 23: 8237–8246.
39. Grob M, Mouginot D (2005) Heterogeneous chloride homeostasis and GABA responses in the median preoptic nucleus of the rat. J Physiol 569: 885–901.
40. Hewitt SA, Wamsteeker JI, Kurz EU, Bains JS (2009) Altered chloride homeostasis removes synaptic inhibitory constraint of the stress axis. Nat Neurosci 12: 438–443.
41. Gulledge AT, Stuart GJ (2003) Excitatory actions of GABA in the cortex. Neuron 37: 299–309.
42. Kaila K, Voipio J, Paalasmaa P, Pasternack M, Deisz RA (1993) The Role of Bicarbonate in $GABA_A$ Receptor-Mediated IPSPs of Rat Neocortical Neurons. J Physiol 464: 273–289.
43. Kaila K (1994) Ionic Basis of $GABA_A$ Receptor-Channel Function in the Nervous-System. Prog Neurobiol 42: 489–537.
44. Kaila K, Pasternack M, Saarikoski J, Voipio J (1989) Influence of GABA-gated bicarbonate conductance on potential, current and intracellular chloride in crayfish muscle-fibers. J Physiol 416: 161–181.
45. Rivera C, Voipio J, Kaila K (2005) Two developmental switches in GABAergic signalling: the K^+-Cl^- cotransporter KCC2 and carbonic anhydrase CAVII. J Physiol 562: 27–36.
46. Sipila ST, Huttu K, Soltesz I, Voipio J, Kaila K (2005) Depolarizing GABA acts on intrinsically bursting pyramidal neurons to drive giant depolarizing potentials in the immature hippocampus. J Neurosci 25: 5280–5289.
47. Staley KJ, Mody I (1992) Shunting of excitatory input to dentate gyrus granule cells by a depolarizing $GABA_A$ receptor-mediated postsynaptic conductance. J Neurophysiol 68: 197–212.
48. Balena T, Acton BA, Koval D, Woodin MA (2008) Extracellular potassium regulates the chloride reversal potential in cultured hippocampal neurons. Brain Res 1205: 12–20.
49. Price TJ, Cervero F, Gold MS, Hammond DL, Prescott SA (2009) Chloride regulation in the pain pathway. Brain Res Rev 60: 149–170.
50. Staley KJ (2004) Role of the depolarizing GABA response in epilepsy. Recent Advances in Epilepsy Research 548: 104–109.
51. Buzsaki G, Kaila K, Raichle M (2007) Inhibition and brain work. Neuron 56: 771–783.
52. Asiedu M, Ossipov MH, Kaila K, Price TJ (2010) Acetazolamide and midazolam act synergistically to inhibit neuropathic pain. Pain 148: 302–308.
53. Knabl J, Witschi R, Hosl K, Reinold H, Zeilhofer UB, et al. (2008) Reversal of pathological pain through specific spinal $GABA_A$ receptor subtypes. Nature 451: 330–3U6.
54. Buhl EH, Tamas G, Szilagyi T, Stricker C, Paulsen O, et al. (1997) Effect, number and location of synapses made by single pyramidal cells onto aspiny interneurones of cat visual cortex. J Physiol 500: 689–713.
55. Tamas G, Buhl EH, Somogyi P (1997) Fast IPSPs elicited via multiple synaptic release sites by different types of GABAergic neurone in the cat visual cortex. J Physiol 500: 715–738.
56. Kaila K, Panula P, Karhunen T, Heinonen E (1991) Fall in intracellular pH mediated by $GABA_A$ receptors in cultured rat astrocytes. Neurosci Lett 126: 9–12.
57. Holmgren CD, Mukhtarov M, Malkov AE, Popova IY, Bregestovski P, et al. (2010) Energy substrate availability as a determinant of neuronal resting potential, GABA signaling and spontaneous network activity in the neonatal cortex in vitro. J Neurochem 112: 900–912.
58. Rheims S, Holmgren CD, Chazal G, Mulder J, Harkany T, et al. (2009) GABA action in immature neocortical neurons directly depends on the availability of ketone bodies. J Neurochem 110: 1330–1338.
59. Ruusuvuori E, Kirilkin I, Pandya N, Kaila K (2010) Spontaneous network events driven by depolarizing GABA action in neonatal hippocampal slices are not attributable to deficient mitochondrial energy metabolism. J Neurosci 30: 15638–15642.
60. Tyzio R, Allene C, Nardou R, Picardo MA, Yamamoto S, et al. (2011) Depolarizing actions of GABA in immature neurons depend neither on ketone bodies nor on pyruvate. J Neurosci 31: 34–45.
61. Glykys J, Dzhala VI, Kuchibhotla KV, Feng G, Kuner T, et al. (2009) Differences in cortical versus subcortical GABAergic signaling: a candidate mechanism of electroclinical uncoupling of neonatal seizures. Neuron 63: 657–672.
62. Bazhenov M, Timofeev I, Steriade M, Sejnowski TJ (2004) Potassium model for slow (2-3 hz) in vivo neocortical paroxysmal oscillations. J Neurophysiol 92: 1116–1132.
63. Frohlich F, Bazhenov M, Iragui-Madoz V, Sejnowski TJ (2008) Potassium dynamics in the epileptic cortex: new insights on an old topic. Neuroscientist 14: 422–433.
64. Carnavale, NT, Hines, ML (2006) The Neuron Book. Cambridge: Cambridge University Press.
65. Lopreore CL, Bartol TM, Coggan JS, Keller DX, Sosinsky GE, et al. (2008) Computational modeling of three-dimensional electrodiffusion in biological systems: Application to the node of Ranvier. Biophys J 95: 2624–2635.
66. Qian N, Sejnowski TJ (1990) When is an inhibitory synapse effective? Proc Natl Acad Sci U S A 87: 8145–8149.
67. Glickfeld LL, Roberts JD, Somogyi P, Scanziani M (2009) Interneurons hyperpolarize pyramidal cells along their entire somatodendritic axis. Nat Neurosci 12: 21–23.
68. De Koninck Y, Mody I (1994) Noise-analysis of miniature IPSCs in adult-rat brain-slices - properties and modulation of synaptic $GABA_A$ receptor channels. J Neurophysiol 71: 1318–1335.
69. Otis TS, Staley KJ, Mody I (1991) Perpetual inhibitory activity in mammalian brain-slices generated by spontaneous GABA release. Brain Res 545: 142–150.
70. Otis TS, De Koninck Y, Mody I (1993) Characterization of synaptically elicited $GABA_B$ responses using patch-clamp recordings in rat hippocampal slices. J Physiol 463: 391–407.
71. Jorgensen PL, Hakansson KO, Karlish SJD (2003) Structure and mechanism of Na,K-ATPase: Functional sites and their interactions. Annu Rev Physiol 65: 817–849.
72. Decker KF, Heijman J, Silva JR, Hund TJ, Rudy Y (2009) Properties and ionic mechanisms of action potential adaptation, restitution, and accommodation in canine epicardium. Am J Physiol Heart circ physiol 296: H1017–H1026.
73. Livshitz LM, Rudy Y (2007) Regulation of Ca^{2+} and electrical alternans in cardiac myocytes: role of CAMKII and repolarizing currents. Am J Physiol Heart circ physiol 292: H2854–H2866.
74. Pasternack M, Voipio J, Kaila K (1993) Intracellular carbonic-anhydrase activity and its role in GABA-induced acidosis in isolated rat hippocampal pyramidal neurons. Acta Physiol Scan 148: 229–231.
75. Lindskog S, Coleman JE (1973) Catalytic mechanism of carbonic-anhydrase. Proc Natl Acad Sci U S A 70: 2505–2508.
76. Katsura K, Mellergard P, Theander S, Ouyang YB, Siesjo BK (1993) Buffer capacity of rat cortical tissue as well as of cultured neurons and astrocytes. Brain Res 618: 283–294.
77. Roberts EL, Chih CP (1998) The pH buffering capacity of hippocampal slices from young adult and aged rats. Brain Res 779: 271–275.
78. Kersh AE, Hartzler LK, Havlin K, Hubbell BB, Nanagas V, et al. (2009) pH regulating transporters in neurons from various chemosensitive brainstem regions in neonatal rats. Am J Physiol Regul Integr Comp Physiol 297: R1409–R1420.
79. Sheldon C, Church J (2002) Na^+/H^+ exchange: molecular regulation to therapeutic development. Clin Invest Med 25: 229–232.
80. Yao H, Ma EB, Gu XQ, Haddad GG (1999) Intracellular pH regulation of CA1 neurons in Na^+/H^+ isoform 1 mutant mice. J Clin Invest 104: 637–645.
81. Hille, B (2001) Ion Channels of Excitable Membranes. Sunderland, Massachussetts: Sinauer Associates. 814 p.
82. Parker GW (2002) Electric field outside a parallel plate capacitor. Am J Phys 70: 502–507.
83. Clay JR (1998) Excitability of the squid giant axon revisited. J Neurophysiol 80: 903–913.
84. Hudmon A, Lebel E, Roy H, Sik A, Schulman H, et al. (2005) A mechanism for Ca^{2+}/calmodulin-dependent protein kinase II clustering at synaptic and nonsynaptic sites based on self-association. J Neurosci 25: 6971–6983.
85. Verkman AS, Sellers MC, Chao AC, Leung T, Ketcham R (1989) Synthesis and characterization of improved chloride-sensitive fluorescent indicators for biological Aapplications. Anal Biochem 178: 355–361.
86. Gilbert D, Franjic-Wurtz C, Funk K, Gensch T, Frings S, et al. (2007) Differential maturation of chloride homeostasis in primary afferent neurons of the somatosensory system. Int J Dev Neuro 25: 479–489.